NASA CONTRACTOR REPORT

VORTICITY INTERACTION EFFECTS ON BLUNT BODIES

E. Clay Anderson and David C. Wilcox

Prepared by
DCW INDUSTRIES
Sherman Oaks, Calif. 91423
for Langley Research Center

NATIONAL AERONAUTICS AND SPACE ADMINISTRATION • WASHINGTON, D. C. • JANUARY 1977

1. Report No.	2. Government Accession No.	3. Recipient's Catalog No.
NASA CR-2778		

4. Title and Subtitle	5. Report Date
VORTICITY INTERACTION EFFECTS ON BLUNT BODIES	January 1977
	6. Performing Organization Code: DW-08

7. Author(s)	8. Performing Organization Report No.
E. Clay Anderson David C. Wilcox	DCW-R-08-01
	10. Work Unit No.

9. Performing Organization Name and Address	11. Contract or Grant No.
DCW Industries 13535 Ventura Boulevard, Suite 207 Sherman Oaks, CA 91423	NAS1-13974
	13. Type of Report and Period Covered: Final Report - 6/1/75-6/1/76

12. Sponsoring Agency Name and Address	14. Sponsoring Agency Code
NASA Langley Research Center Hampton, VA 23365	

15. Supplementary Notes

Langley technical monitor: Kenneth Sutton

Final report.

16. Abstract

A two-part study of hypersonic viscous shock layers has been conducted. In the first part of the study, numerical solutions of the viscous-shock-layer equations governing laminar and turbulent flows of a perfect gas and radiating and non-radiating mixtures of perfect gases in chemical equilibrium are presented for hypersonic flow over spherically blunted cones and hyperboloids. Turbulent properties are described in terms of the classical mixing length. Results are compared with boundary-layer and inviscid flowfield solutions; agreement with inviscid flowfield data is satisfactory. Agreement with boundary-layer solutions is good except in regions of strong vorticity interaction; in these flow regions, the viscous-shock-layer solutions appear to be more satisfactory than the boundary-layer solutions. The second part focuses upon preparation for future applications; boundary conditions suitable for hypersonic viscous shock layers are devised for an advanced turbulence theory.

17. Key Words (Suggested by Author(s))	18. Distribution Statement
Viscous Shock Layer; Radiation Gasdynamics Boundary Layer; Turbulence Model; Streamline Swallowing; Vorticity Interaction;	Unclassified - Unlimited Subject Category 02

19. Security Classif. (of this report)	20. Security Classif. (of this page)	21. No. of Pages	22. Price*
Unclassified	Unclassified	70	$4.25

*For sale by the National Technical Information Service, Springfield, Virginia 22151

CONTENTS

CONTENTS (concluded)

NOTATION

SYMBOL	DEFINITION
A^+	Damping factor [Equations (15) and (16)]
C_i	Mass fraction of species i, ρ_i/ρ
C_ℓ	Mass fraction of element ℓ
C_p	Frozen specific heat of mixture, $\sum_{i=1}^{N} C_i C_{p,i}$
$C_{p,i}$	Specific heat of species i, $C^*_{p,i}/C^*_{p,\infty}$
c^*	Inviscid flow velocity gradient
e	Turbulent mixing energy
H	Defined quantity, $h + \frac{u^2}{2}$
H_t	Total enthalpy, $H + \frac{v^2}{2}$
h	Enthalpy of mixture, $\sum_{i=1}^{N} C_i h_i$
h_A	Enthalpy of undecomposed ablation material
h_i	Enthalpy of species i, h^*_i/U^{*2}_∞
I_e, I_w	Intermittency factors
j	Flow index: 0 for plane flow; 1 for axisymmetric flow
K	Thermal conductivity of mixture, $K^*/\mu^*_{ref}\ C^*_{p,\infty}$
k	Roughness height
k^+	Roughness height Reynolds number, $\rho_w u_\tau k/\mu_w$
ℓ	Turbulent length scale
$\tilde{\ell}$	Mixing length [Equation (13)]
M^*	Molecular weight
$\overline{M}^*$	Molecular weight of mixture
N	Number of species

NOTATION (continued)

SYMBOL	DEFINITION
N_{Le}	Lewis number, $\rho^* D^*_{ij} C^*_p / K^*$
$N_{Le,T}$	Turbulent Lewis number
N_{Pr}	Prandtl number, $\mu^* C^*_p / K^*$
$N_{Pr,T}$	Turbulent Prandtl number, $\mu^*_T C^*_p / K^*_T$
N_{Re}	Reynolds number, $\rho^*_\infty U^*_\infty r^*_n / \mu^*_\infty$
N_{Sc}	Schmidt number, $N_{Sc} = N_{Pr}/N_{Le}$
n	Coordinate measured normal to body, n^*/r^*_n
n^+	Normal coordinate [Equation (14)]
P^+	Pressure-gradient parameter [Equation (17)]
p	Pressure, $p^*/[\rho^*_\infty (U^*_\infty)^2]$
Q	Divergence of net radiant heat flux, $Q^* r^*_n / \rho^*_\infty U^{*3}_\infty$
q_r	Net radiant heat flux in n-direction, $q^*_r / \rho^*_\infty U^{*2}_\infty$
$q_r^{(+)*}$	Component of radiant flux toward the shock
$q_r^{(-)*}$	Component of radiant flux toward the wall
$-q_{c,w}$	Convective heat flux to the wall [Equation (11)]
Re_D	Reynolds number based on body diameter
r	Radius measured from axis of symmetry to point on body surface, r^*/r^*_n
r^*_n	Nose radius
$\bar{S}$	Production rate [Equation (33)]
$S_B(v^+_w)$	Universal function of surface mass-injection
$S_R(k^+)$	Universal function of surface roughness
s	Coordinate measured along body surface, s^*/r^*_n
T	Temperature, T^*/T^*_{ref}
T^*_{ref}	Temperature, $(U^*_\infty)^2/C^*_{p,\infty}$

NOTATION (continued)

SYMBOL	DEFINITION
U_∞^*	Freestream velocity
u	Velocity component tangent to body surface, u^*/U_∞^*
u_τ	Friction velocity [Equation (19)]
v	Velocity component normal to body surface, v^*/U_∞^*
v_e^*	Entrainment velocity
v_w^+	Scaled mean velocity component [Equation (18)], v_w/u_τ
w	Turbulent dissipation rate
$\tilde{\alpha}$	Shock angle defined in Figure 1
α, α^*	Parameters in turbulence model equations
$\alpha_\infty, \alpha_\infty^*$	High Reynolds number values of α, α^*
$\tilde{\beta}$	Angle defined in Figure 1
β, β^*	Parameters in turbulence model equations
$\gamma_{i,\eta}$	Normal intermittency factor [Equation (22)]
δ	Boundary-Layer thickness
δ_k	Incompressible displacement thickness [Equation (21)]
$\delta_{i\ell}$	Number of atoms of the ℓth element in species i
ε^+	Normalized eddy viscosity, μ_T/μ
ε_i^+	Eddy viscosity, inner law [Equation (12)]
ε_o	Eddy viscosity, outer law [Equation (20)]
η	Transformed n-coordinate, n/n_s; also, similarity coordinate for stagnation-point solution
θ	Body angle defined in Figure 1
κ	Body curvature
μ	Molecular viscosity, $\mu^*/\mu^*(T_{ref}^*)$
μ_T	Eddy viscosity

SYMBOL	DEFINITION
ξ	Coordinate measured along body surface, $\xi = s$; also, similarity coordinate for stagnation-point solution
ρ	Density of mixture, ρ^*/ρ^*_∞
$\tilde{\sigma}$	Reynolds number parameter, $\left[\frac{\mu^*(T^*_{ref})}{\rho^*_\infty U^*_\infty r^*_n}\right]^{\frac{1}{2}}$
$\tilde{\sigma}^*$	Stefan-Boltzmann constant
σ, σ^*	Parameters in turbulence model equations
$\phi_{1,2,3}$	Quantities defined by Equations (4b,4c,4d)

Superscripts

j	0 for plane flow; 1 for axisymmetric flow
-	Quantity divided by its corresponding shock value
*	Dimensional quantity
'	Total differential or fluctuating component
"	Shock-oriented velocity component (see Figure 1)

Subscripts

e	Boundary-layer edge
i	i^{th} species
ℓ	ℓ^{th} element
s	Shock
w	Wall
∞	Freestream
-	Values for the solid ablation material at the surface

Abbreviations

BL	Boundary layer
BLSSW	Boundary layer corrected for streamline swallowing
TFD	Transient finite difference
VSL	Viscous shock layer

VORTICITY INTERACTION EFFECTS ON BLUNT BODIES

E. Clay Anderson* and David C. Wilcox†
DCW Industries

1. INTRODUCTION

Vorticity interaction between the boundary layer and the outer inviscid entropy layer is not significant for high Reynolds number laminar flows over blunt bodies having low angle afterbodies except at distances far downstream. However, for large angle afterbodies such as those being considered for planetary entry probes,[1] vorticity interaction is strong in the region near the nose of the body if the flow is turbulent. For free-stream conditions which require an analysis including mass injection at the surface, vorticity interaction can be a significant influence for laminar flows if the mass injection rate is sufficiently large. As a result of the high speeds associated with typical planetary entry trajectories, radiation heat-transfer effects must also be included in the flowfield analysis.

The use of higher order boundary-layer theory for the analysis of flowfields with a high degree of coupling between the boundary layer (BL) and the inviscid flow requires a complex interative solution procedure. Because of the difficulties experienced in the application of higher order BL theory, Davis[2,3] has developed a numerical technique for solving the viscous-shock-layer (VSL) equations governing laminar flow of a perfect gas and for binary mixtures with finite rate chemical reactions. Moss[4] has developed VSL solutions for multicomponent gas mixtures for both equilibrium and finite rate chemistry. Moss[5] has

*Consultant

†Owner

extended the equilibrium chemistry analysis to include the effects of radiation heat transfer. These VSL analyses have been found accurate for flows with strong vorticity interaction and/or radiation heat transfer.

In recent publications by Eaton and Larson[6] and Anderson and Moss,[7] numerical solutions of the VSL equations governing turbulent flow of a perfect gas have been presented. Eaton and Larson considered the thin VSL equations and presented solutions for turbulent flow over slender cones. Their results were compared with experimental data and showed good agreement. Anderson and Moss considered turbulent flow over blunt axially symmetric bodies and used the full VSL equations. These solutions were compared with first-order turbulent BL theory. The results obtained with this turbulent BL analysis were essentially identical to first-order turbulent BL results in the region where vorticity interaction is not significant. For the downstream region, the expected differences were obtained.

In a later investigation, Anderson and Moss[8] extended the turbulent VSL analysis to reacting gas mixtures in chemical equilibrium and considered both radiating and nonradiating shock layers. These turbulent VSL solutions were compared with first-order BL solutions and first-order BL theory with corrections for streamline swallowing (BLSSW). A nonradiating shock-layer solution corresponding to a typical trajectory point for a Venusian entry was considered. A coldwall boundary condition was assumed, and the results of the VSL analysis were compared with integral BL and BLSSW analyses. The two BL solutions and the VSL solution showed excellent agreement in the laminar flow region. For the turbulent flow region, both the BLSSW and the VSL solution showed a large increase in the heat-transfer rate when compared with the BL solution. For the turbulent flow region, the VSL heat-transfer

rates were 15% to 30% lower than the solution obtained with the integral BLSSW analysis, but the general trend in the heat-transfer rate distribution was the same for both methods of analysis.

For the more complex case of a radiating shock layer with mass injection at the surface, a typical trajectory point for a Venusian entry was analyzed. These VSL results were compared with an integral matrix BLSSW analysis. For this case, the laminar flow region solutions differed by 10% to 15% in convective heating rate predictions, and for the turbulent flow region, the two methods of analysis showed opposite trends in the convective-heating-rate distribution. The BLSSW analysis predicted a maximum convective heating rate at the transition point. The VSL analysis predicted the maximum convective heating rate at a downstream location. For the predominantly inviscid outer flow region of the shock layer, the VSL solution was found to be in satisfactory agreement with the inviscid flowfield solution. The prediction of radiation heating at the surface was in satisfactory agreement with the BLSSW analysis.

The opposite trends in the calculated convective heating-rate distributions appeared to be the result of an increase in vorticity interaction caused by mass injection and the higher temperature at the surface boundary. This behavior was not obtained for the nonradiating case with no injection and cold-wall boundary conditions. The coldwall boundary condition results in a thinner BL thickness and diminishes the influence of vorticity interaction. Both higher surface temperature and mass injection increase vorticity interaction.

The present investigation is directed primarily toward determining the behavior of BLSSW and VSL solutions in regions of strong vorticity interaction. The study consists of two parts.

In the first part of the study, a perfect gas is considered, and the eddy viscosity modeling techniques are identical in both the VSL and BLSSW analyses. Representative VSL profile data are compared with two different inviscid flowfield solutions and BL and BLSSW solutions. VSL solutions are also presented for both radiating and nonradiating mixtures of perfect gases in chemical equilibrium, but comparative BL and BLSSW data are not available for the radiating shock-layer calculations. The second part of the study focuses upon development of an advanced turbulence model in preparation for future viscous shock layer applications.

2. MIXING LENGTH APPLICATIONS

In this section, hypersonic viscous shock layer solutions are presented. The equations of motion appropriate for shock layers are stated, including boundary conditions and assumed thermodynamic properties. The mixing-length closure approximations are then discussed. The solution method is described next. Results of numerical computations are then presented for both perfect-gas and equilibrium radiating gas mixture applications.

2.1 GOVERNING EQUATIONS

The equations of motion for reacting gas mixtures in chemical equilibrium are presented by Bird, Stewart, and Lightfoot.[9] The formulation of these equations in body-oriented coordinates appropriate for viscous-shock-layer analysis of laminar flow of radiating and nonradiating gases is presented by Moss.[4,5] For turbulent flow, the viscous-shock-layer equations are derived using methods analogous to those presented by Dorrance[10] for the turbulent-boundary-layer equations and are expressed in nondimensional form for the coordinate system shown in Figure 1 as:

Continuity:

$$\frac{\partial}{\partial s}[(r + n\cos\theta)^j \rho u] + \frac{\partial}{\partial n}[(1 + n\kappa)(r + n\cos\theta)^j \rho v] = 0 \qquad (1)$$

s- momentum:

$$\rho\left(\frac{u}{1+n\kappa}\frac{\partial u}{\partial s} + v\frac{\partial u}{\partial n} + \frac{uv\kappa}{1+n\kappa}\right) + \frac{1}{1+n\kappa}\frac{\partial p}{\partial s} = \tilde{\sigma}^2\left\{\frac{\partial}{\partial n}\left[\mu(1+\varepsilon^+)\frac{\partial u}{\partial n} - \frac{\mu u\kappa}{1+n\kappa}\right]\right.$$
$$\left. + \left(\frac{2\kappa}{1+n\kappa} + \frac{j\cos\theta}{r + n\cos\theta}\right)\left[\mu(1+\varepsilon^+)\frac{\partial u}{\partial n} - \frac{\mu u\kappa}{1+n\kappa}\right]\right\} \qquad (2)$$

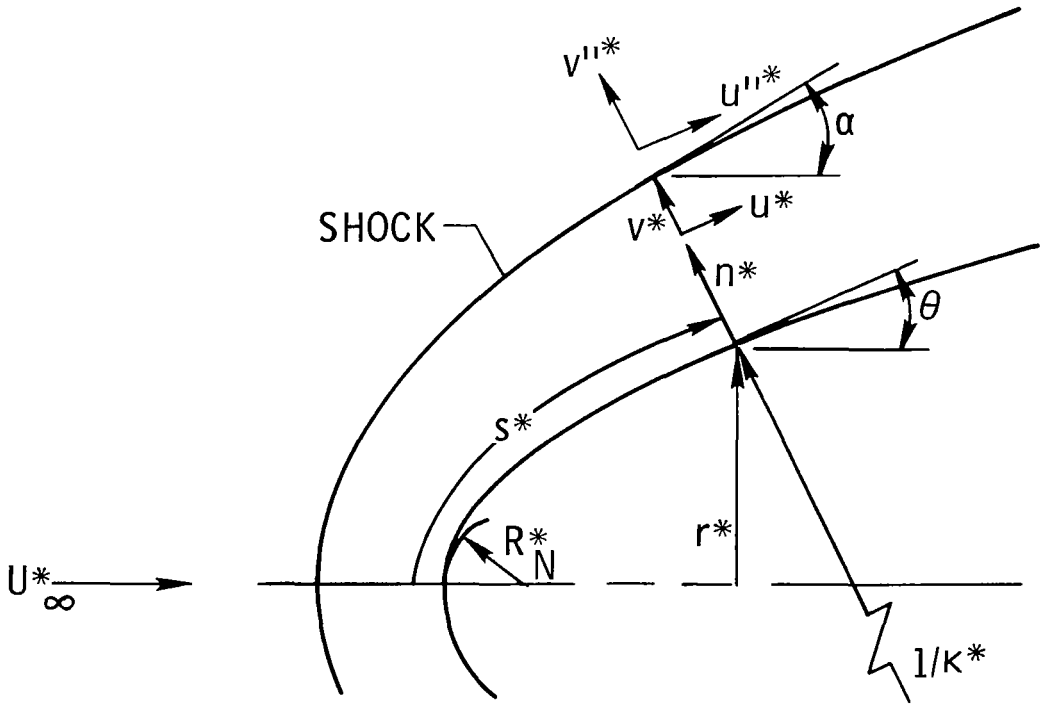

Figure 1. Coordinate system.

n-momentum:

$$\rho\left(\frac{u}{1+n\kappa}\frac{\partial v}{\partial s} + v\frac{\partial v}{\partial n} - \frac{u^2\kappa}{1+n\kappa}\right) + \frac{\partial p}{\partial n} = 0 \tag{3}$$

Energy:

$$\rho\left(\frac{u}{1+n\kappa}\frac{\partial H}{\partial s} + v\frac{\partial H}{\partial n}\right) - v\frac{\partial p}{\partial n} + \frac{\rho u^2 v\kappa}{1+n\kappa}$$

$$= \tilde{\sigma}^2\left[\frac{\partial}{\partial n}(\phi_1+\phi_2+\phi_3) + \left(\frac{\kappa}{1+n\kappa} + \frac{j\cos\theta}{r+n\cos\theta}\right)(\phi_1+\phi_2+\phi_3)\right] - Q \tag{4a}$$

where

$$\phi_1 = \frac{\mu}{N_{Pr}}\left(1 + \varepsilon^+ \frac{N_{Pr}}{N_{Pr,T}}\right)\frac{\partial H}{\partial n} \tag{4b}$$

$$\phi_2 = \frac{\mu}{N_{Pr}}\left[N_{Pr} - 1 + \frac{\varepsilon^+ N_{Pr}}{N_{Pr,T}}\left(N_{Pr,T} - 1\right)\right]u\frac{\partial u}{\partial n} - \frac{\mu u^2\kappa}{1+n\kappa} \tag{4c}$$

$$\phi_3 = \frac{\mu}{N_{Pr}}\left[N_{Le} - 1 + \varepsilon^+ \frac{N_{Pr}}{N_{Pr,T}}\left(N_{Le,T} - 1\right)\right]\sum_{i=1}^{N} h_i \frac{\partial C_i}{\partial n} \tag{4d}$$

and

$$H \equiv h + \frac{u^2}{2} \tag{4e}$$

Elemental continuity:

$$\rho\left(\frac{u}{1+n\kappa}\frac{\partial \tilde{C}_\ell}{\partial s} + v\frac{\partial \tilde{C}_\ell}{\partial n}\right) = \frac{\tilde{\sigma}^2}{(1+n\kappa)(r+n\cos\theta)^j}$$

$$\times \frac{\partial}{\partial n}\left\{\left[(1+n\kappa)(r+n\cos\theta)^j \frac{\mu}{N_{Pr}}\left(N_{Le} + \varepsilon^+ \frac{N_{Pr}}{N_{Pr,T}}N_{Le,T}\right)\frac{\partial \tilde{C}_\ell}{\partial n}\right]\right\} \tag{5a}$$

where

$$\tilde{C}_\ell = \sum_{i=1}^{N} \delta_{i\ell}\frac{M_\ell^*}{M_i^*}C_i \tag{5b}$$

State:

$$p = \rho T R^*/\bar{M}^* C^*_{p,\infty} \tag{6}$$

2.1.1 Boundary Conditions

The boundary conditions at the shock are calculated by using the Rankine- Hugoniot relations. At the wall, the no-slip and no-temperature-jump boundary conditions are used; consequently, $u_w = 0$. The wall temperature and mass injection rate are either specified or calculated. For the calculated mass injection conditions, the ablation process is assumed to be quasi-steady and the wall temperature is the sublimation temperature of the ablator surface. With these assumptions, the expression for the coupled mass injection rate is

$$\dot{m} = \left(\frac{-q^*_{c,w} - q^*_{r,w}}{\sum_{i=1}^{N} (\dot{C}_i h^*_i)_w - h^*_A} \right) \left(\frac{1}{\rho^*_\infty U^*_\infty} \right) \tag{7}$$

For ablation injection, the elemental concentrations at the wall are governed by convection and diffusion as given by the equation

$$\left(\frac{\partial \tilde{C}_\ell}{\partial n} \right)_w - \frac{1}{\tilde{\sigma}^2} \left(\frac{\dot{m} N_{Sc}}{\mu} \right)_w \left[\left(\tilde{C}_\ell \right)_w - \left(\tilde{C}_\ell \right)_- \right] = 0 \tag{8}$$

Precursor effects are neglected while the energy reradiated from the surface is included in the radiation transport calculations. The net radiative flux, q_r, can be represented as the difference of two components

$$q_r = q_r^{(+)} - q_r^{(-)} \tag{9}$$

At the surface

$$q_{r,w}^{(+)*} = \varepsilon \tilde{\sigma}^* T_w^{*4} \tag{10}$$

where ε is the surface emissivity.

The heat transferred to the wall due to conduction and diffusion is

$$-q_{c,w} = \tilde{\sigma}^2 \left(K \frac{\partial T}{\partial n} + \frac{\mu}{N_{Sc}} \sum_{i=1}^{N} h_i \frac{\partial C_i}{\partial n} \right)_w \tag{11}$$

2.1.2 Radiative Transport

The radiative flux, q_r, is calculated with the radiative transport code RAD.[11,12] The RAD computer code has been incorporated in the present viscous-shock-layer computer code (HYVIS) and streamlined for computational efficiency.

The RAD code accounts for the effects of nongray self-absorption. Molecular band, continuum, and atomic line transitions are included. A detailed frequency dependence of the absorption coefficients is used for integrating over the radiation frequency spectrum and the tangent slab approximation is used for integrating over physical space.

2.1.3 Thermodynamic and Transport Properties

The equilibrium composition is determined by a free energy minimization calculation as developed in Reference 13. Thermodynamic properties for specific heat, enthalpy, and free energy and transport properties for viscosity and thermal conductivity are required for each species considered. Values for the thermodynamic[14,15] and transport properties[16] are obtained by using polynomial curve fits. The mixture viscosity is obtained by using the semiempirical formula of Wilke.[17]

2.2 EDDY-VISCOSITY APPROXIMATIONS

A two-layer eddy-viscosity model consisting of an inner law based upon Prandtl's mixing-length concept and the Clauser-Klebanoff expression (based on References 18 and 19) for the outer law is used in the present investigation. This model, introduced by Cebeci,[20] assumes that the inner law is applicable for the flow from the wall out to the location where the eddy viscosity given by the inner law is equal to that of the outer law. The outer law is then assumed applicable for the remainder of the viscous layer. It is noted that the eddy viscosity degenerates to approximately zero in the inviscid portion of the shock layer. The degeneracy is expressed in terms of the normal intermittency factor given by Klebanoff.[19] The expressions used in the present investigation are given in the following sections.

2.2.1 Inner-Eddy-Viscosity Approximation

Prandtl's mixing-length concept is stated in nondimensional variables as

$$\varepsilon_i^+ = \frac{\rho \tilde{\ell}^2}{\tilde{\sigma}^2 \mu} \left| \frac{\partial u}{\partial n} \right| \tag{12}$$

The mixing length, $\tilde{\ell}$, is evaluated by using van Driest's[21] proposal stated as

$$\tilde{\ell} = k_1 n \left[1 - \exp\left(- \frac{n^+}{A^+} \right) \right] \tag{13}$$

where

$$n^+ = \frac{n\rho}{\tilde{\sigma}\mu} \left[\frac{\mu_w}{\rho} \left(\frac{\partial u}{\partial n} \right)_w \right]^{1/2} \tag{14}$$

Here, k_1 is the von Karman constant, which is assumed to have a value of 0.4, and A^+ is a damping factor whose value is 26.

Cebeci[20] suggests that for flows with a pressure gradient, the damping factor be expressed as

$$A^+ = 26(1 - 11.8P^+)^{-\frac{1}{2}} \tag{15}$$

and for flows with both a pressure gradient and mass injection,

$$A^+ = 26\left\{-\frac{P^+}{v_w^+}[\exp(11.8v_w^+) - 1] + \exp(11.8v_w^+)\right\}^{-\frac{1}{2}} \tag{16}$$

where

$$P^+ = -\tilde{\sigma}^2\left(\frac{\partial p}{\partial s}\right)_e \frac{\mu}{\rho^2 u_\tau^3} \tag{17}$$

$$v_w^+ = \frac{v_w}{u_\tau} \tag{18}$$

and

$$u_\tau = \tilde{\sigma}\left[\frac{\mu_w}{\rho}\left(\frac{\partial u}{\partial n}\right)_w\right]^{\frac{1}{2}} \tag{19}$$

2.2.2 Outer-Eddy-Viscosity Approximation

For the outer region of the viscous layer the eddy viscosity is approximated by the Clauser-Klebanoff expression

$$\varepsilon_o^+ = \frac{k_2 \rho u_e \delta_k \gamma_{i,n}}{\tilde{\sigma}^2 \mu} \tag{20}$$

where $k_2 = 0.0168$ and δ_k and $\gamma_{i,n}$ are defined as

$$\delta_k = \int_o^\delta \left(1 - \frac{u}{u_e}\right) dn \tag{21}$$

and

$$\gamma_{i,\eta} = \left[1 + 5.5\left(\frac{\eta}{\delta}\right)^6\right]^{-1} \tag{22}$$

Equation (22) is Cebeci's[20] approximation of the error-function definition presented by Klebanoff.[19]

For equilibrium flow without radiation, the boundary-layer thickness δ is assumed to be the value of n at the point where

$$\frac{H_t}{H_{t,\infty}} = 0.995 \tag{23}$$

and is defined by linear interpolation in an array of local total enthalpies. This definition is approximately equivalent to the usual boundary-layer definition

$$\frac{u}{u_e} = 0.995 \tag{24}$$

where u_e is the local value for the undisturbed inviscid flow outside the boundary layer.

The values of the parameters k_1 and k_2 in Equations (13) and (20) depend on the flow conditions being considered, as does the constant represented by the value 26 in Equations (15) and (16). The values given are used for convenience in developing the numerical method. A discussion of these parameters is presented by Harris.[22]

For radiating gases, the loss of energy from the shock layer makes the total enthalpy definition unsatisfactory. For these cases, the boundary-layer thickness is assumed to be defined by an index of diffusion, conduction, and dissipation expressed as

$$\frac{\int_0^{\delta} \left| \frac{\partial}{\partial n}(\phi_1+\phi_2+\phi_3) + \left(\frac{\kappa}{1+n\kappa} + \frac{j \cos\theta}{r + n\cos\theta} \right)(\phi_1+\phi_2+\phi_3) \right| dn}{\int_0^{N_S} \left| \frac{\partial}{\partial n}(\phi_1+\phi_2+\phi_3) + \left(\frac{\kappa}{1+n\kappa} + \frac{j \cos\theta}{r + n\cos\theta} \right)(\phi_1+\phi_2+\phi_3) \right| dn} = 0.95 \quad (25)$$

Boundary-layer thicknesses given by this expression are essentially the same as those given by the total enthalpy definition when applied to perfect gas flows, but both definitions overpredict the BL thickness in the vicinity of the stagnation streamline when an equilibrium gas is considered.

For the present study, the turbulent Prandtl and Lewis numbers are assumed to be 0.9 and 1.0, respectively.

2.3 SOLUTION METHOD

Davis[2] presented a method for solving the viscous-shock-layer equations for stagnation and downstream flow. Moss[4,5] applied this method of solution to reacting multicomponent mixtures. The present method of solution is identical to that of References 2 and 4. Therefore, only an overview of the solution procedure is presented here.

The numerical computation is simplified by normalizing most of the variables with their local shock values. The transformed independent and dependent variables are

$$\left.\begin{array}{ll} \eta = n/n_s & \bar{p} = p/p_s \\ \xi = s & \bar{\rho} = \rho/\rho_s \\ \bar{u} = u/u_s & \bar{T} = T/T_s \\ \bar{v} = v/v_s & \bar{H} = H/H_s \\ \bar{\mu} = \mu/\mu_s & \bar{K} = K/K_s \end{array}\right\} \quad (26)$$

Since the normal coordinate, n, is normalized with respect to the local shock standoff distance, a constant number of finite-difference grid points between the body and shock are used. The transformations relating the differential quantities are

$$\frac{\partial}{\partial s} = \frac{\partial}{\partial \xi} - \frac{n_s'}{n_s} \eta \frac{\partial}{\partial \eta} \tag{27a}$$

where

$$n_s' = \frac{dn_s}{d\xi} \tag{27b}$$

$$\frac{\partial}{\partial n} = \frac{1}{n_s} \frac{\partial}{\partial \eta} \tag{27c}$$

and

$$\frac{\partial^2}{\partial n^2} = \frac{1}{n_s^2} \frac{\partial^2}{\partial \eta^2} \tag{27d}$$

The second-order partial differential equations are linearized and written in the standard form for a parabolic equation as

$$\frac{\partial^2 W}{\partial \eta^2} + \alpha_1 \frac{\partial W}{\partial \eta} + \alpha_2 W + \alpha_3 + \alpha_4 \frac{\partial W}{\partial \xi} = 0 \tag{28}$$

where W represents tangential velocity for the s-momentum equation, enthalpy for the energy equation, and elemental concentrations for the elemental continuity equations. For the energy equation, the divergence of the radiative flux is included in the α_3 term. When the derivatives in Equation (28) are converted to finite-difference form by using Taylor's series expansions, the resulting equations are of the following form:

$$A_n W_{m,n-1} + B_n W_{m,n} + C_n W_{m,n+1} = D_n \tag{29}$$

The subscript n denotes the grid points along a line normal to the body surface, and the subscript m denotes the grid stations along the body surface. Equation (29), along with the boundary conditions, constitute a system of the tridiagonal form and can be solved efficiently.

A variable grid spacing is used in both the tangential and normal directions to the surface so that the grid spacing can be made small in the region of large gradients. The order of the truncation terms neglected are $\Delta\xi$ (first order accurate) and either $\Delta\eta_n\Delta\eta_{n-1}$ or $(\Delta\eta_n - \Delta\eta_{n-1})$.

The equations are solved at any body station m in the order shown in Figure 2. The governing equations are uncoupled and the values of the dependent variables are computed one at a time. Each of the second-order differential equations is individually integrated numerically by using the tridiagonal formalism [Equation (29)]. The global continuity equation is used to obtain both shock standoff distance and the $\bar{v}$ components of velocity. By integrating the global continuity equation between the limits of 0 to 1, a quadratic equation for n_s is obtained. For the $\bar{v}$ component of velocity at η, the global continuity equation is integrated with respect to η between the limits of 0 to η. The pressure, p, is determined at station m by integrating the normal momentum equation with respect to η between the limits of 1 to η. The equation of state is used to determine the density. The solution is iterated until convergence is achieved. The solution advances to the next body station, m + 1, and uses the previous converged solution profiles as initial values for starting the solution at station m + 1. This procedure is repeated until a solution pass is obtained.

The first solution pass provides a first approximation to the flowfield solution because the following assumptions are used.

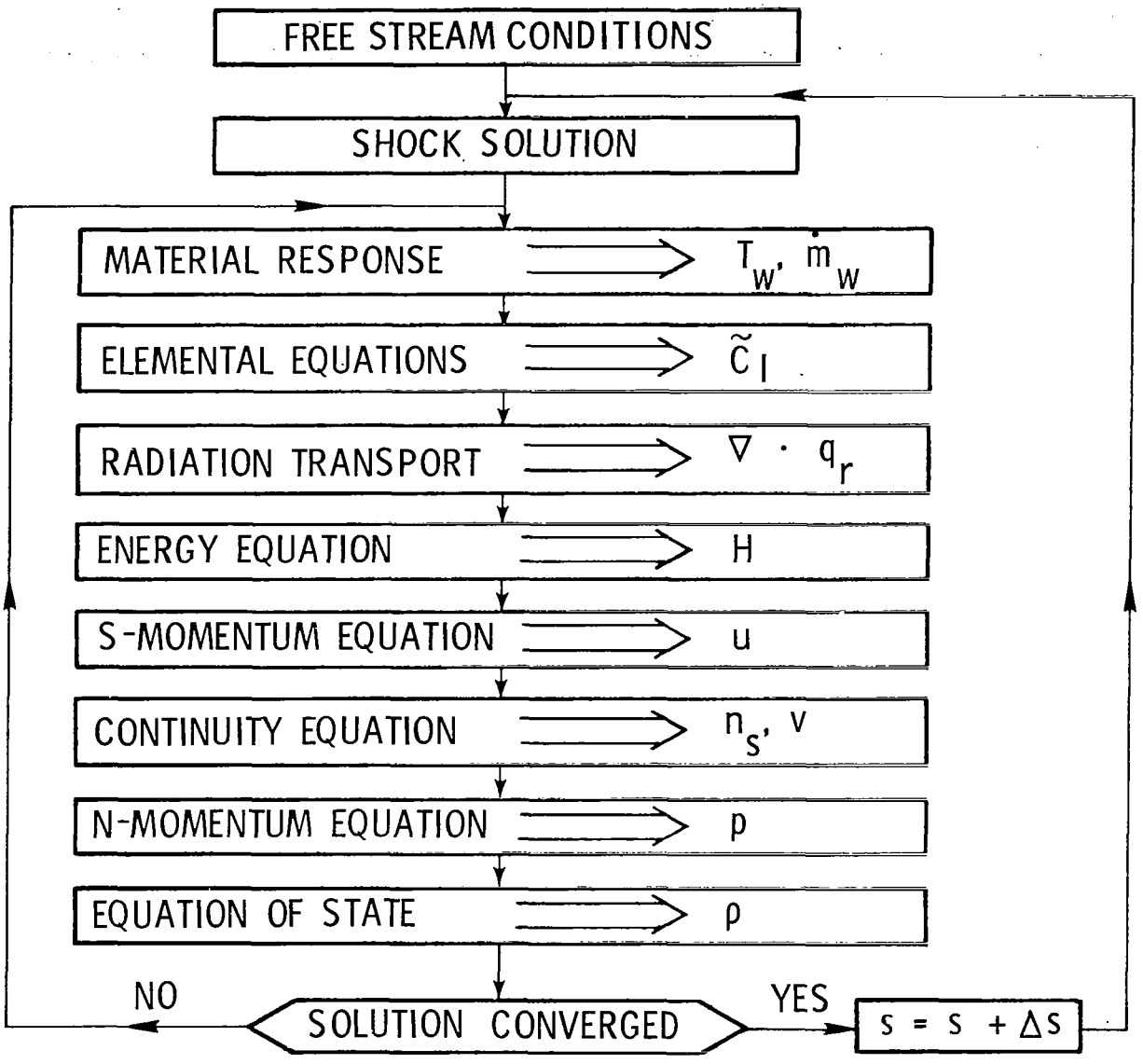

Figure 2. Flow design of local solution procedure.

The thin shock-layer form of the n-momentum equation, $\frac{\kappa\rho u^2}{1+n\kappa} = \frac{\partial p}{\partial n}$, is used; the stagnation streamline solution is independent of downstream influence; the term $dn_s/d\xi$ is set to zero at each body station, and the shock angle α is assumed to be the same as the body angle θ. These approximations are then removed by global iteration. Two solution passes are generally sufficient. This solution procedure is programmed for the CDC 6600 computer.

2.4 RESULTS AND DISCUSSION

Numerical solutions of the VSL equations governing laminar, transitional, and turbulent flows of a perfect gas are compared with inviscid, BL, and BLSSW solutions. Equivalent but less extensive comparisons are presented for nonradiating mixtures of perfect gases in chemical equilibrium. VSL solution data are also presented for a radiating mixture of perfect gases in chemical equilibrium but comparative data are not available for this case.

2.4.1 Perfect Gas Solutions with Strong Vorticity Interaction

VSL solutions for laminar and turbulent flow of a Mach 10 free-stream over a 40° half-angle spherically blunted cone are presented. Representative profile data obtained using the VSL analysis are compared with inviscid, BL, and BLSSW profile data. The inviscid flowfield solutions were obtained using the blunt-body method of characteristics (MOC) of Inouye, et al,[23] and the transient finite-difference (TFD) procedure of Sutton.[24] The BL data were obtained using the analysis of Anderson and Lewis.[25] BLSSW data were obtained using the analysis of Mayne and Dyer[26] (this solution was provided by Dr. Arloe W. Mayne, Jr. of ARO, Inc.), and the analysis of Reference 25 was modified to account for variable entropy edge conditions during the present investigation.

Surface pressure distributions corresponding to the VSL and MOC solutions are shown in Figure 3. Excellent agreement is obtained except in the vicinity of the sphere-cone tangency point where differences are ±10%. These differences have little influence upon the downstream flow and are not excessive in the region near the tangency point. The shock shapes corresponding to the VSL and MOC solutions are essentially identical and are not presented.

Figure 4 shows heating-rate distributions corresponding to (1) the BL analysis of Reference 25, (2) the BLSSW analysis of Reference 26, (3) VSL solutions corresponding to the assumptions that the BL edge is located as defined by either Equation (23) or (25) and at the bow shock, and (4) laminar VSL and BLSSW (Reference 25) solutions. For turbulent flow, instantaneous transition at $s = 0.8$ has been assumed, and the damping factor, A^+, in the van Driest eddy viscosity law is assumed to be 26 in all calculations.

The turbulent VSL solution with the BL edge location defined by either Equation (23) or (25) and using Equation (22) for $\gamma_{i,\eta}$ is in excellent agreement with the BL analysis of Reference 25 for $s \leq 2.5$. In the region of strong vorticity interaction, the heating rates predicted by the VSL solution are as much as 40% less than the heating rates predicted by the two BLSSW solutions. In the downstream region where the inviscid entropy layer has been swallowed by the BL, the VSL and BLSSW solutions approach an equivalent cone solution, as they should.

The turbulent VSL solution is strongly influenced by the definition of the BL edge location. To demonstrate the maximum influence of the BL edge definition on the VSL solution, the BL edge was assumed to be located at the bow shock and a unit value for $\gamma_{i,\eta}$ was assumed. These assumptions result in maximum

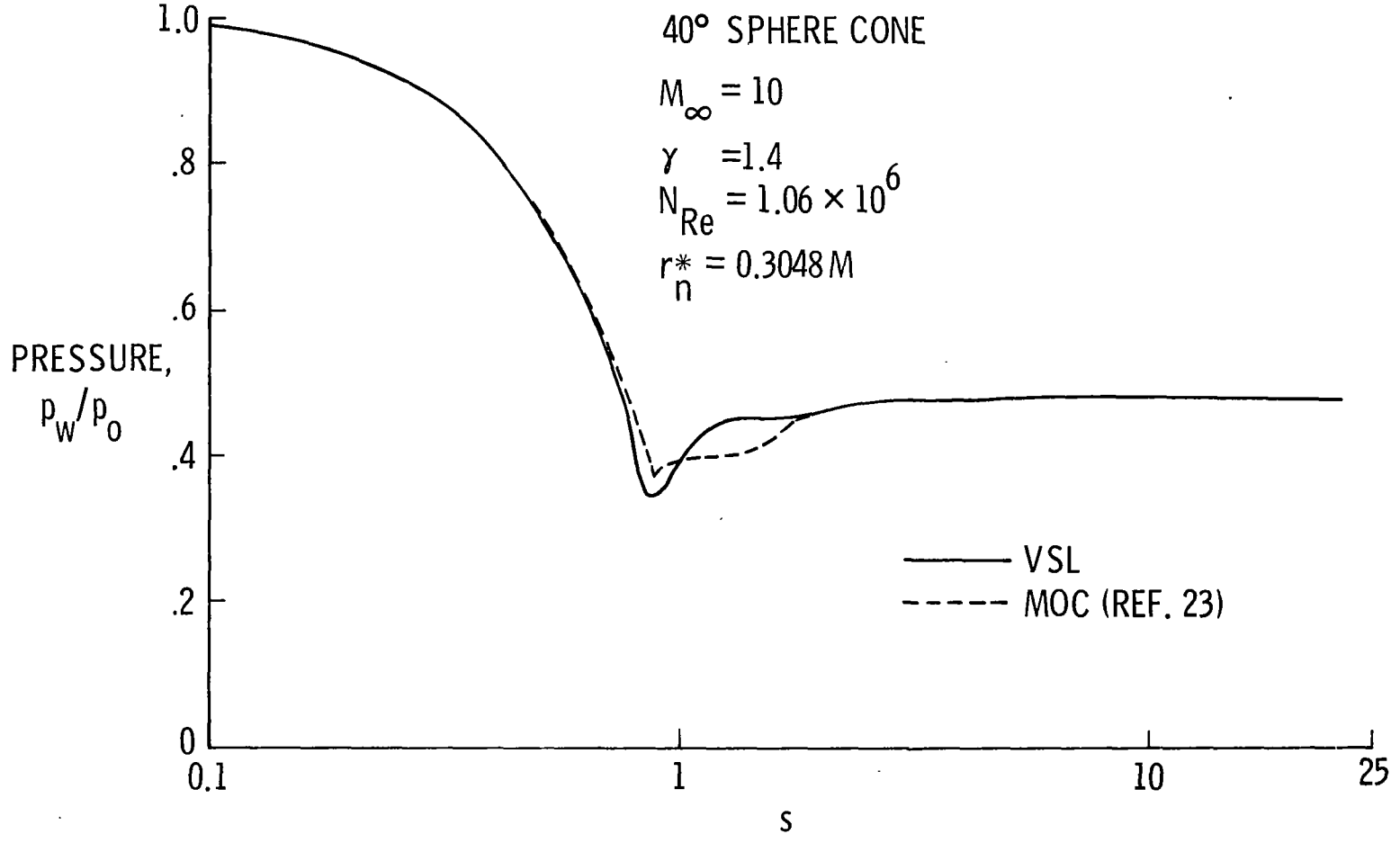

Figure 3. Surface pressure distributions.

BL SOLUTIONS

LAM	TURB	NORMAL INTERMITTANCY	ENTROPY CORRECTION	REF.
----			YES	25
	----	1	YES	26
	- - - -	EQN. 22	YES	25
	———	EQN. 22	NO	25

VSL SOLUTIONS

LAM	TURB	NORMAL INTERMITTANCY	BL EDGE LOCATION

	• • •	1	AT SHOCK
	+ + +	EQN. 22	$H_t/H_{t,\infty} = 0.995$

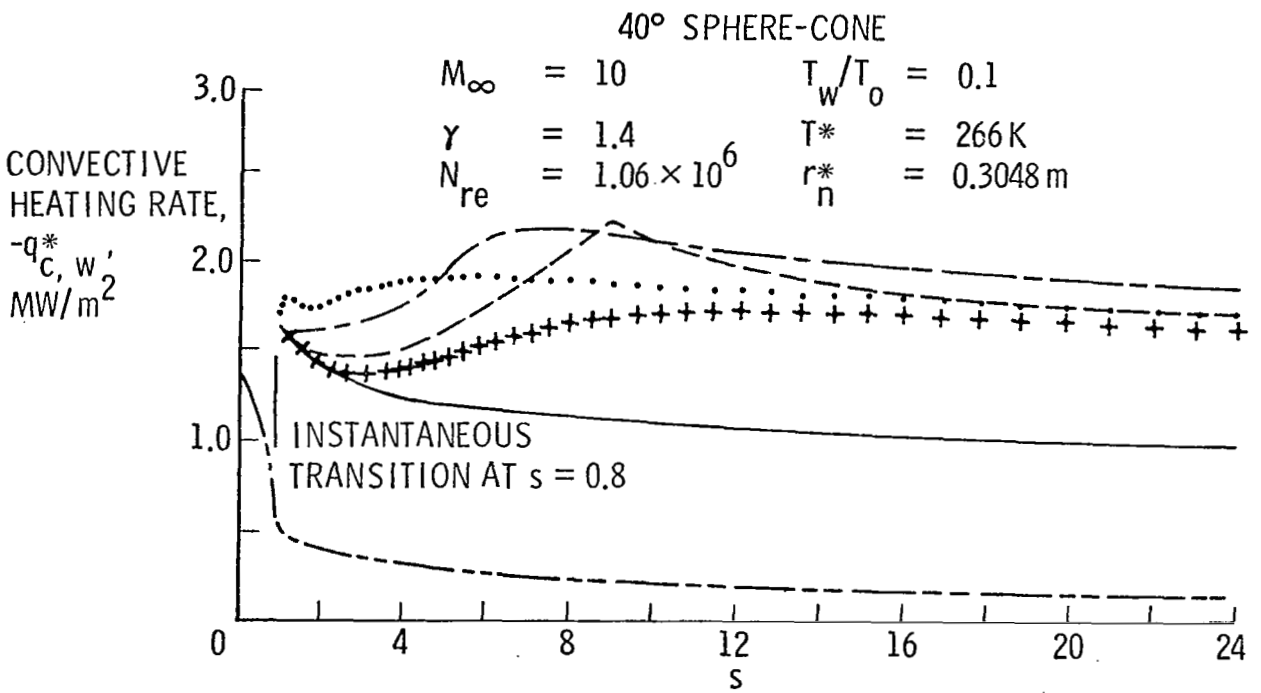

Figure 4. Heating-rate distributions.

eddy viscosities using the present mixing length turbulence model. This solution shows the expected behavior, but the peak heating rates predicted by the VSL solution remains substantially less than that given by the BLSSW solutions. The laminar VSL and BLSSW[25] solutions which are not directly influenced by the BL and the displacement thicknesses show excellent agreement (±3%) for the heating-rate distribution. The data presented are the VSL solution.

The apparent contradiction for the agreement between laminar and turbulent VSL and BLSSW solutions is the result of the BL and the displacement thickness distributions obtained using the BLSSW analyses. Both BLSSW solutions showed a linear increase in the BL and the displacement thickness distributions up to the point where the inviscid entropy layer is swallowed by the BL. Downstream of this point, these thickness distributions showed a gradual decrease in magnitude until the equivalent cone solution was approached. Since these definitions determine the scale for turbulence, the turbulent-heat-rate distributions predicted by the BLSSW solutions show the same behavior.

The rapid growth of the BL and displacement thickness in the region where longitudinal entropy gradients were significant was obtained for both laminar and turbulent flow when the variable entropy corrections presented by Blottner[27] were used in the analysis of Reference 25. An approximate streamline swallowing analysis which corrected only the edge conditions was also used. This approach has been used by Price and Harris[28] and was found to give a more satisfactory distribution for the BL and the displacement thicknesses. The heat-transfer-rate distribution obtained with this approximate analysis was essentially the same as when the full modifications presented by Blottner[27] were used. A more accurate BL solution would require higher-order theory (see van Dyke[29]).

Figure 5 shows velocity profile data at four locations. The VSL solutions are compared with the inviscid flowfield solutions of References 23 and 24, the BLSSW solution of Reference 26, and the BL solution of Reference 25. At s = 2.1, the VSL profile data in the inner viscous region show good agreement with both BL and BLSSW solutions for turbulent flow. However, as is evident from the different heating rates predicted at this station, the temperature profiles corresponding to the BLSSW solution showed pronounced differences from that of the VSL solution. The temperature profiles corresponding to the BL solution show good agreement with the VSL solution as indicated by the heating-rate prediction. These data are not presented.

In the predominantly inviscid outer flow region, the VSL profile data show satisfactory agreement (±5%) with both inviscid flowfield solutions. The VSL and TFD solutions do not show the distinct sharp peak in the velocity profile that is a characteristic of spherically blunted cone flowfields as shown by the MOC results. Since TFD inviscid flowfield solutions generally use less than 15 interior grid points across the shock layer, the differences between the TFD and MOC solutions are probably the result of inadequate resolution. The VSL solutions were obtained using 150 interior grid points with approximately 80 points within the predominantly viscous inner region and the remaining 70 points in the predominantly inviscid outer region. Since velocity and temperature gradients are relatively large in the inviscid entropy layer, the differences between the MOC and VSL solutions appear to be the result of viscous and displacement effects.

Profile data at s = 3.2 and 6.7 show that the agreement between the VSL and BLSSW solution becomes progressively worse as vorticity increases at the BL edge. After the inviscid entropy layer is swallowed by the viscous layer, the agreement between

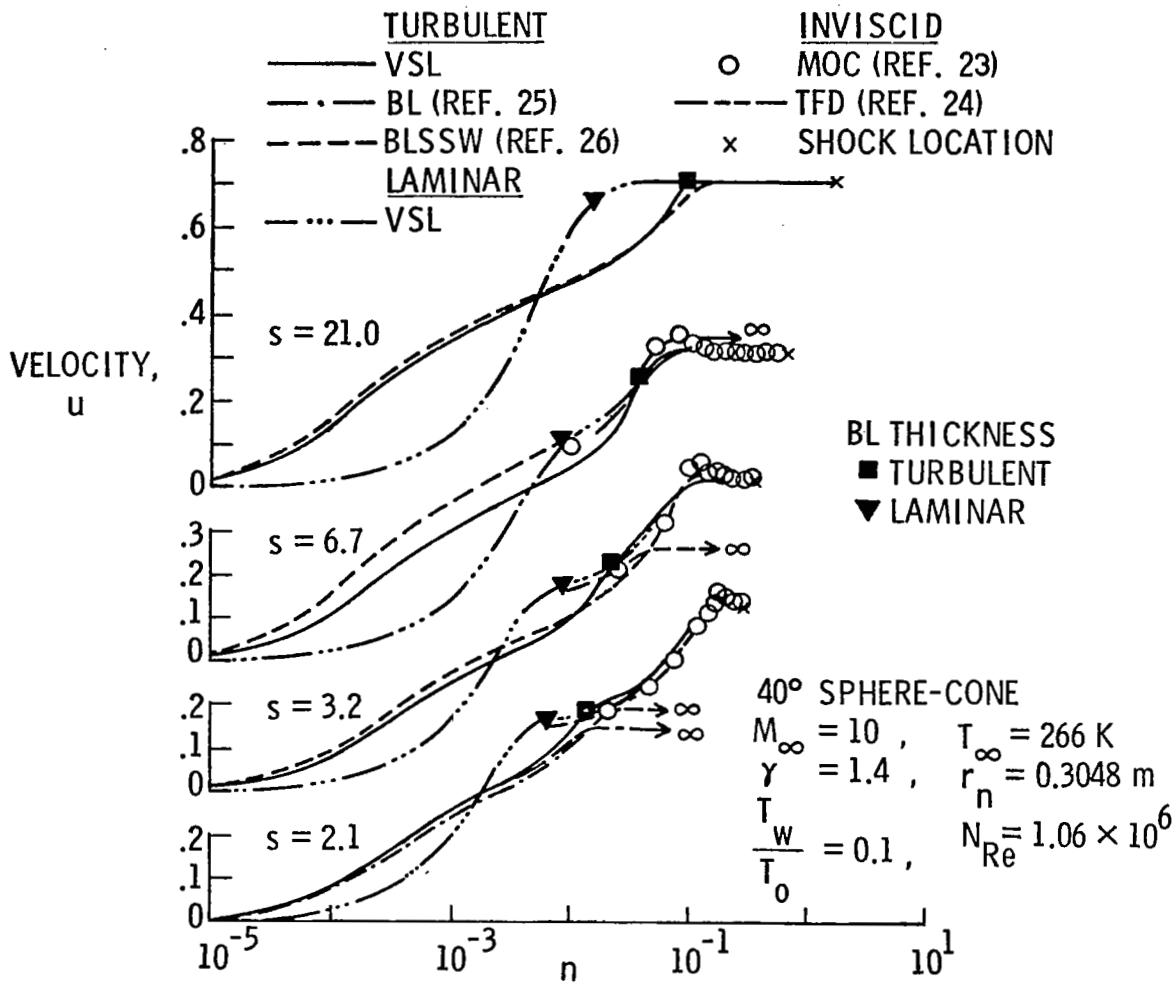

Figure 5. Comparisons of velocity profiles.

the two methods of solution is satisfactory as shown at s = 21. The profile data at s = 6.7 show that the inviscid entropy layer has been swallowed by the BL using the BLSSW analysis. The VSL profile data show a distinct "inviscid entropy layer," and these data are in satisfactory agreement with both inviscid flowfield solutions.

The solutions presented for the 40° half-angle spherically blunted cone indicate that the VSL solution procedure is satisfactory for high Reynolds number laminar and turbulent flows. The VSL solutions using algebraic mixing length turbulence models in conjunction with the definition expressed by either Equation (23) or Equation (25) for the BL edge location show acceptable agreement with BL solutions in the nose region of blunt bodies and with BLSSW solutions in the far downstream flow. The solutions appear to be more satisfactory than BLSSW solutions for flows with strong vorticity interaction. However, the accuracy of the present solution procedure and the applicability of the algebraic mixing length turbulence modeling technique in the presence of strong vorticity interaction must be determined by experimental verification. Turbulence models which are independent of conventional boundary-layer thickness definitions are needed for the present method of analysis.

2.4.2 Solutions for Radiating and Nonradiating Gas Mixtures in Chemical Equilibrium

A VSL solution for the flowfield over a 60° half-angle spherically blunted cone for a typical Venusian entry trajectory point is presented in Figures 6 and 7. The VSL solution is compared with BL and BLSSW solutions obtained using the integral analysis of Edquist[30] (this solution was provided by C.T. Edquist, Martin-Marietta Corp., Denver Division).

The inviscid flowfield solution used to specify edge conditions for the BL and BLSSW solutions was determined using a single

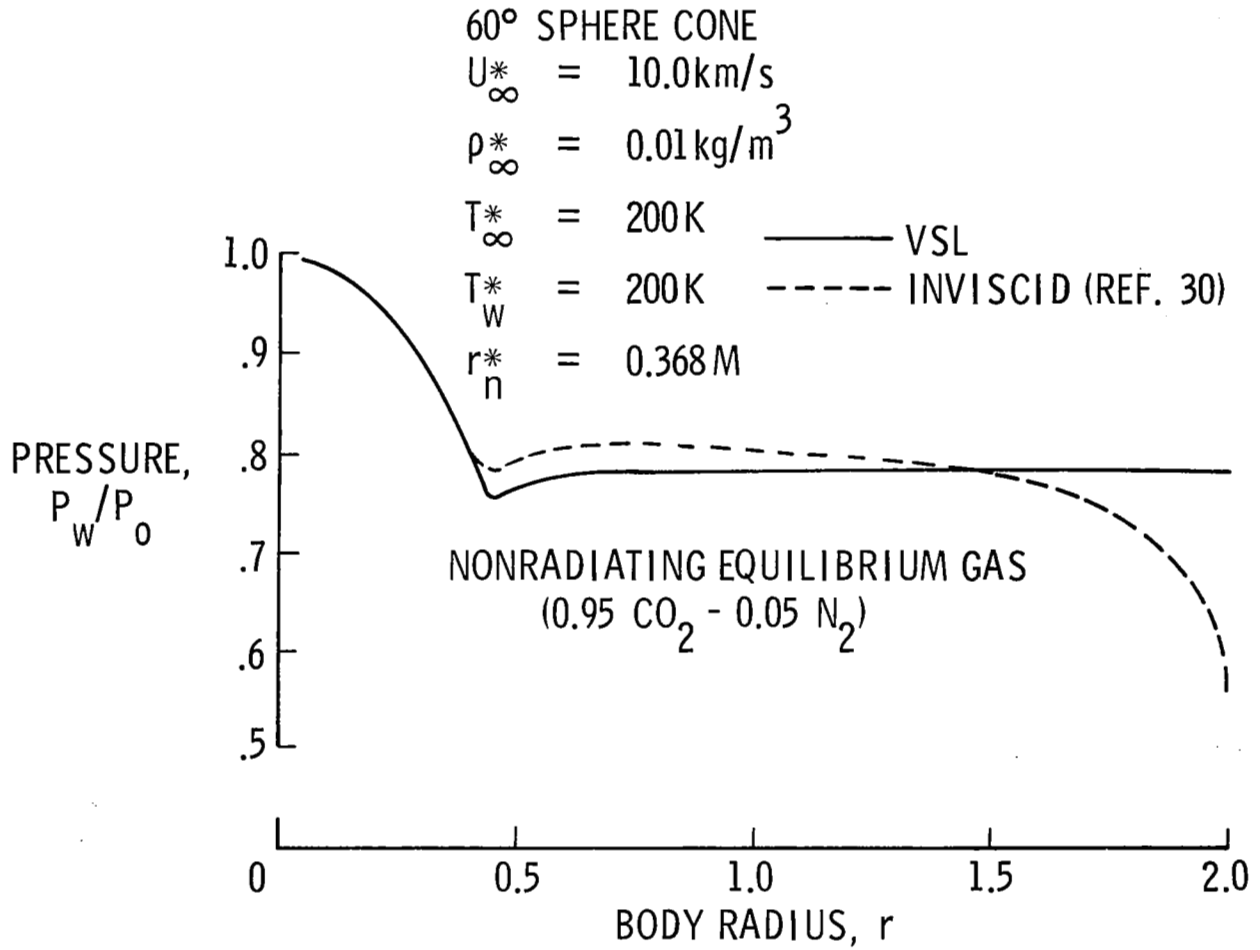

Figure 6. Surface pressure distributions.

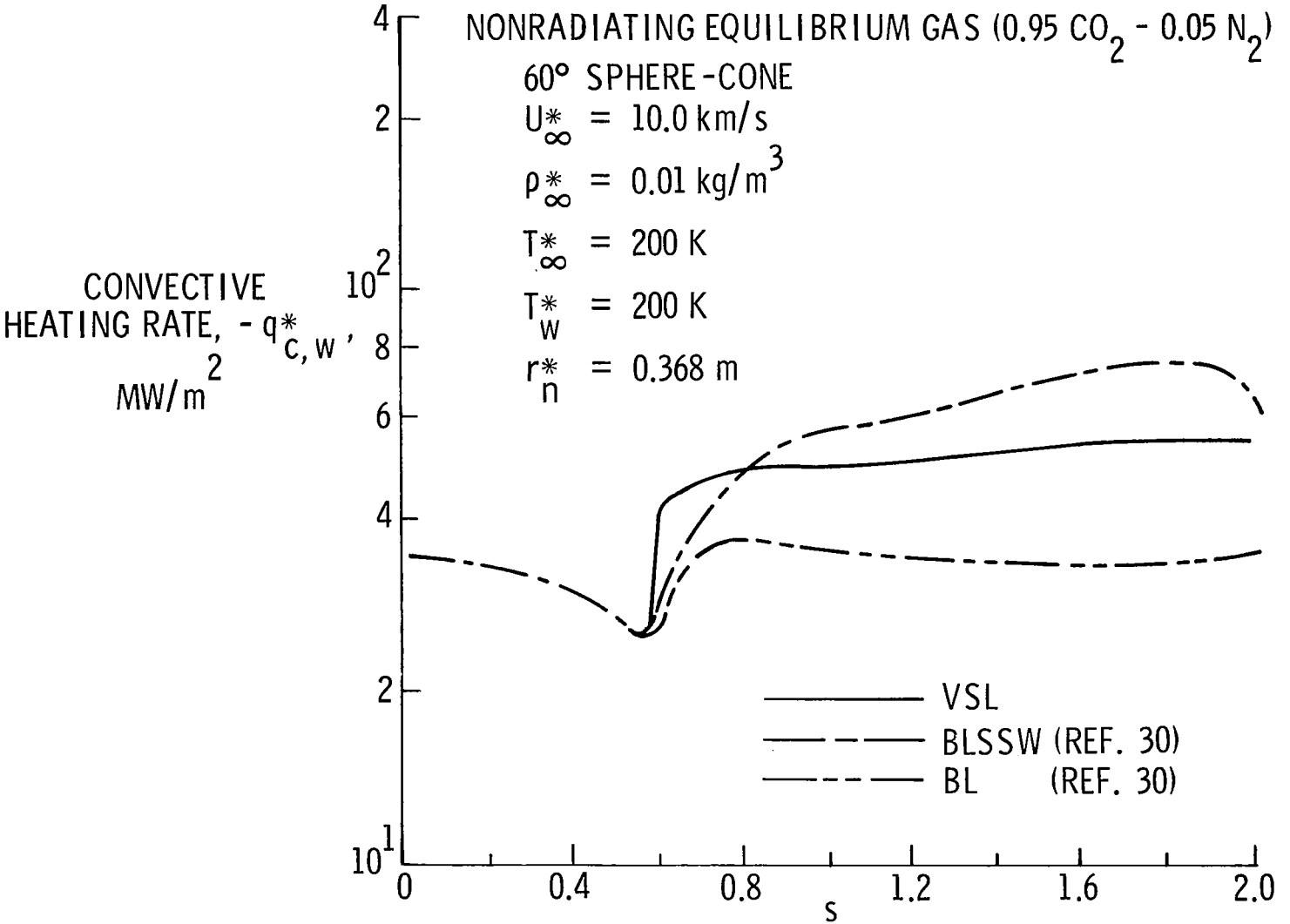

Figure 7. Heating-rate distributions.

strip integral method which accounts for the upstream influence of the sonic corner. The present formulation of the VSL equations cannot account for this influence. The surface pressure distributions corresponding to the two methods of analysis are shown in Figure 6. The influence of the sonic corner is significant only in the region $1.6 \leq r < 2$. For $r \leq 1.6$, the maximum difference between the two methods of analysis is less than 4%.

Convective heat-transfer rate distributions corresponding to the integral BL and BLSSW solutions and the present VSL solution are presented in Figure 7. The present solution corresponds to assuming instantaneous transition from laminar to turbulent flow with either Equation (23) or Equation (25) used for the BL edge definition and Equation (22) for the normal intermittency factor. The convective heat-transfer rate correlation formula used in the BL and BLSSW solutions includes a transition correction. The BLSSW and VSL solutions show the expected influence of vorticity interaction, but the VSL solution predicts heating rates that are approximately 30% lower than that given by the BLSSW solution. These differences are approximately the same as those obtained in the region of strong vorticity interaction for the previously discussed perfect gas solutions. For the present problem, these differences are not excessive and are generally to be expected when comparing different numerical techniques using different turbulence models. For the laminar flow region, the different solution procedures are in excellent agreement.

VSL solution results are presented in Figures 8-11 for a 40° half-angle hyperboloid for freestream conditions corresponding to a typical Jovian entry trajectory point. Wall shear-stress and convective heating-rate distributions are compared with the solution obtained using the BL analysis of Bartlett and

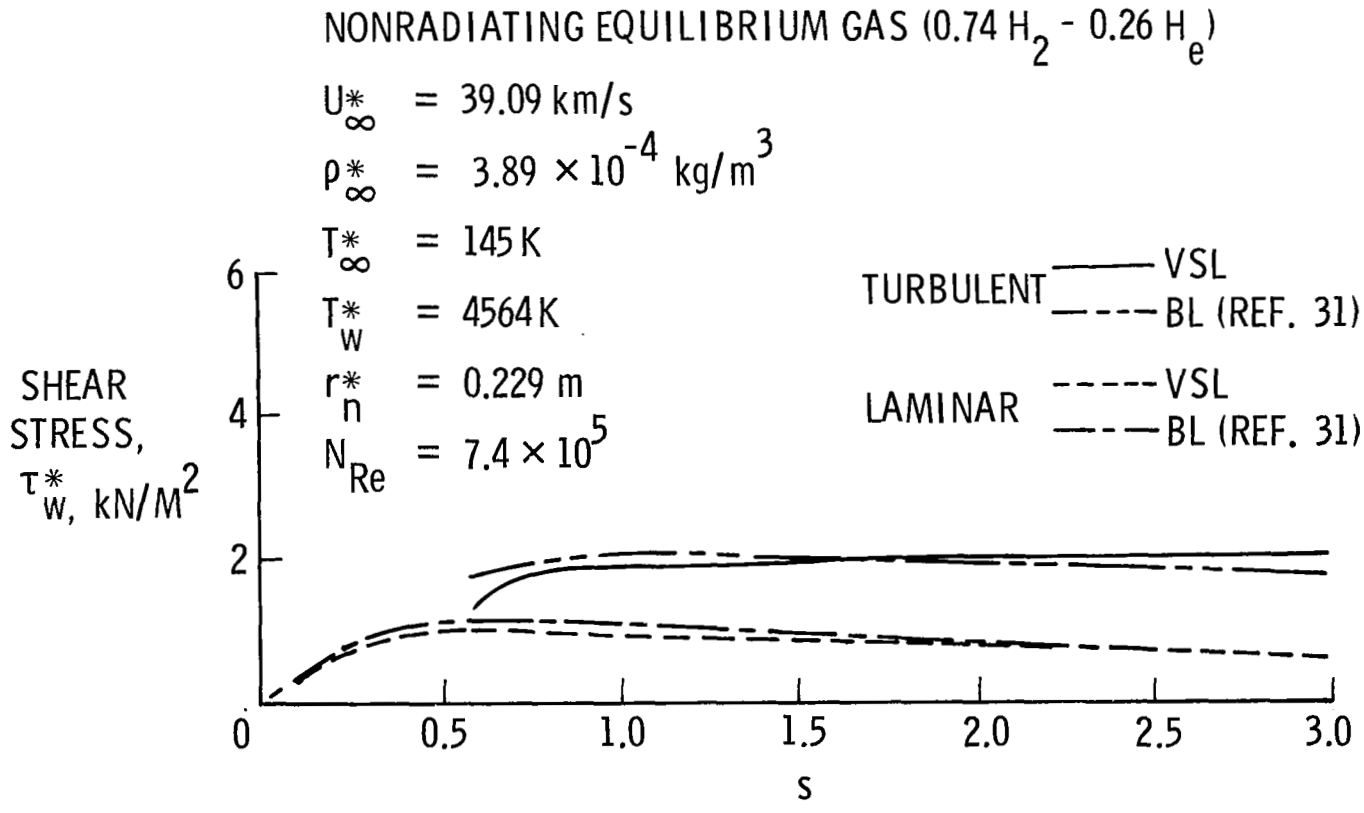

Figure 8. Wall shear stress distribution for a 40° hyperboloid.

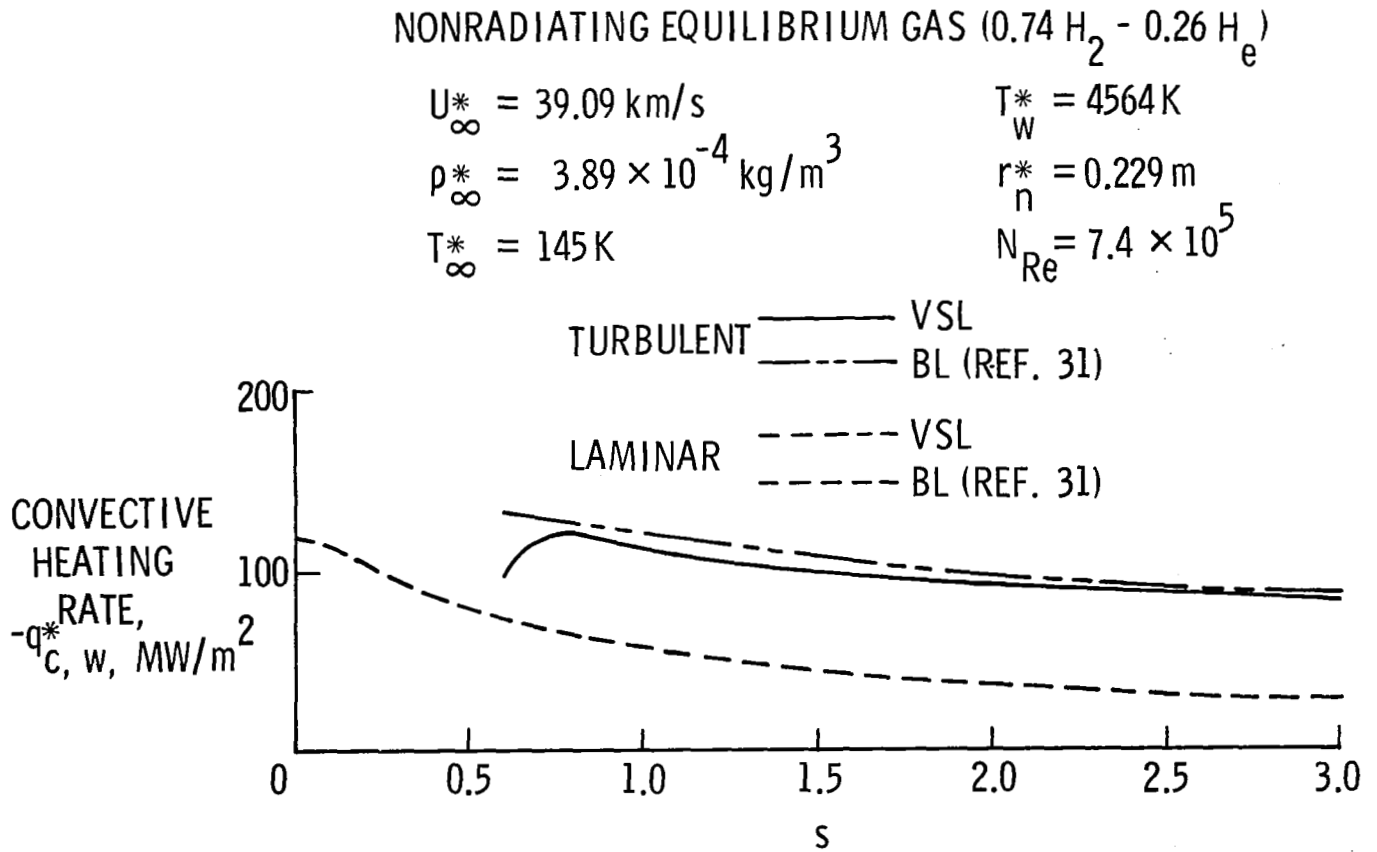

Figure 9. Heating-rate distribution for a 40° hyperboloid.

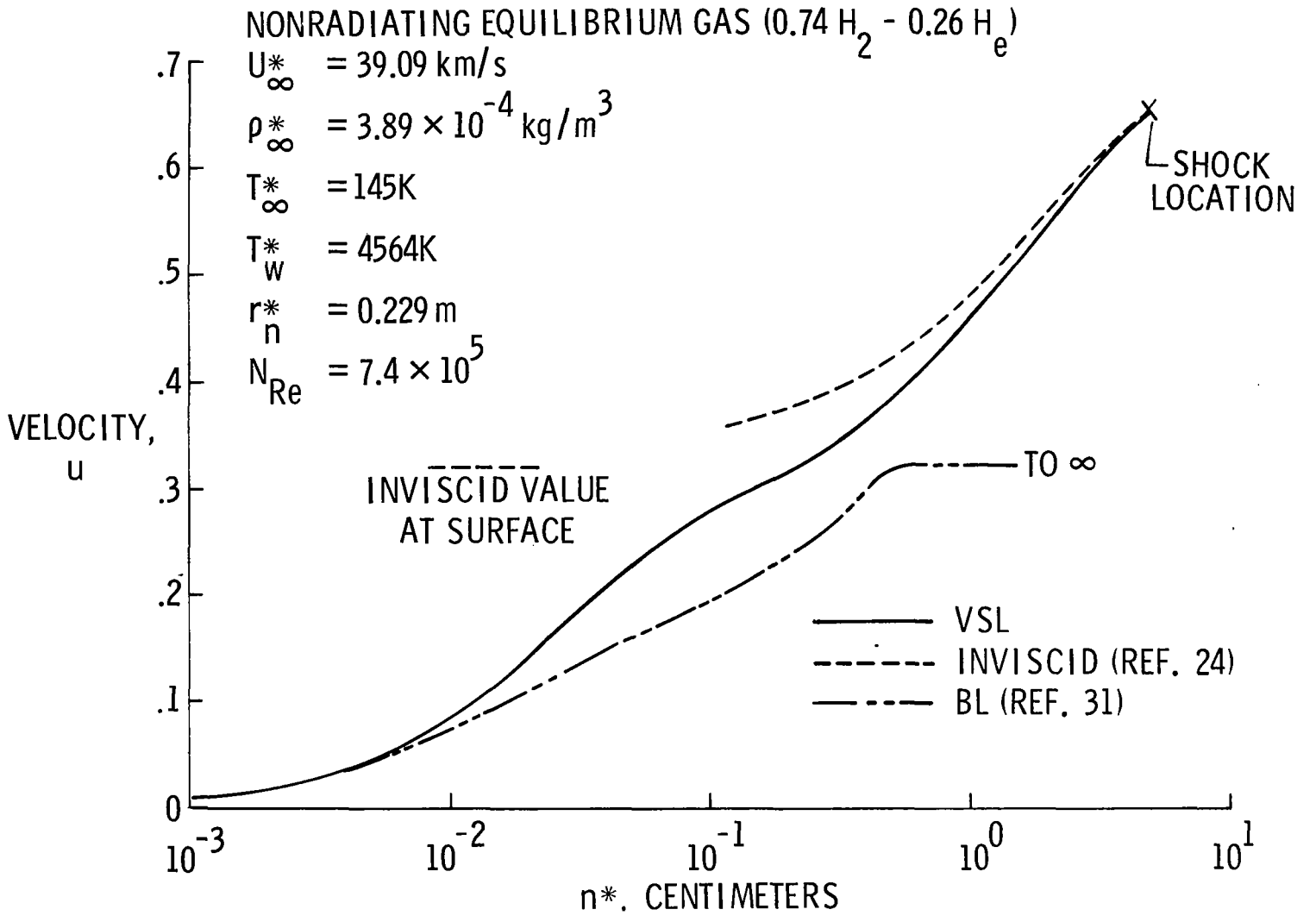

Figure 10. Turbulent velocity profiles at s = 2 for a 40° hyperboloid.

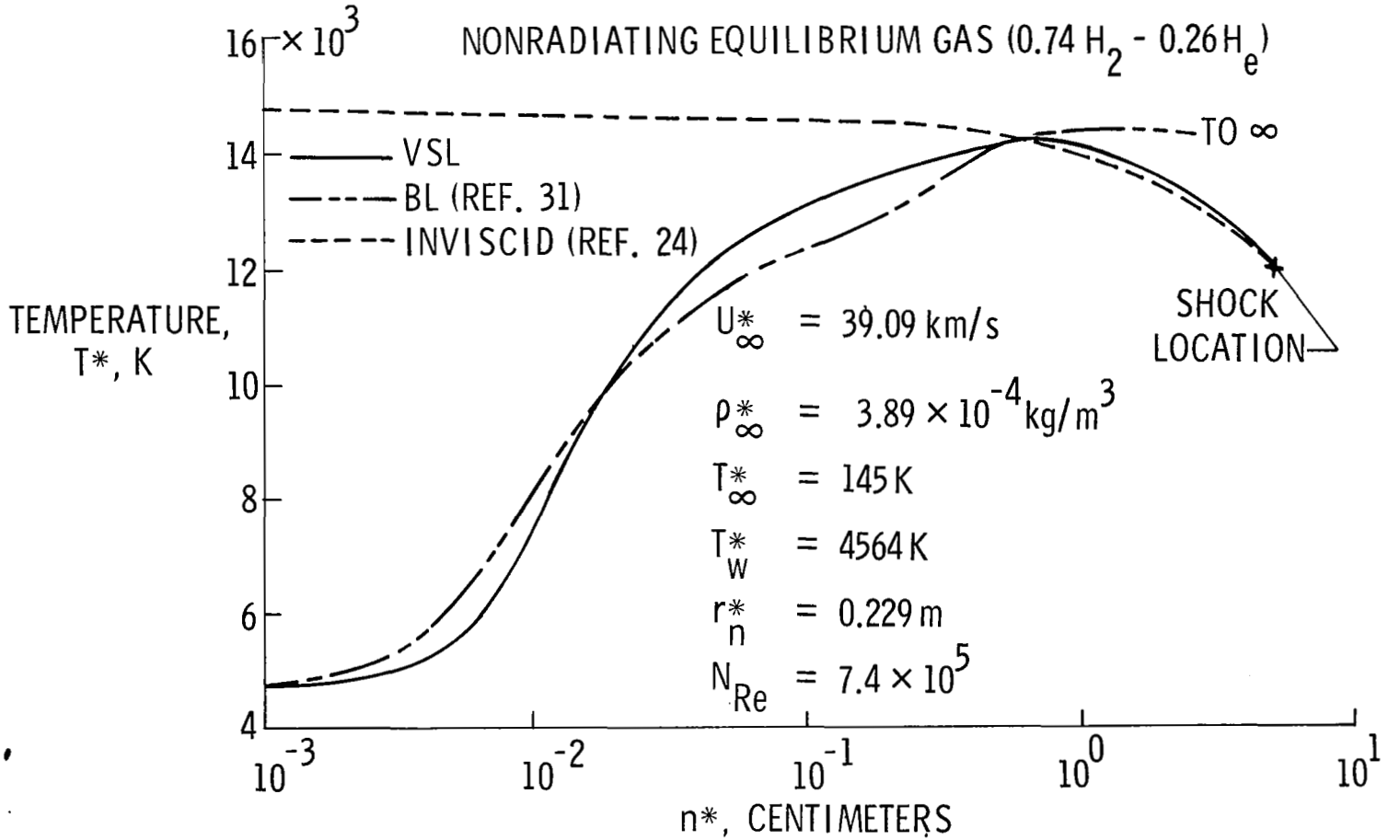

Figure 11. Temperature profiles at s = 2 for a 40° hyperboloid.

Kendall.[31] The inviscid constant entropy edge conditions for this BL solution were determined using the TFD procedure of Reference 24.

Wall shear-stress and convective heating-rate distributions are shown in Figures 8 and 9, respectively. With the exception of the region near the point of instantaneous transition from laminar to turbulent flow, the wall shear-stress distributions for both laminar and turbulent flow show differences of less than ±10%. Laminar convective heating-rate distributions are essentially identical and are shown as a single curve, and for turbulent flow, the two methods of analysis differ by ±5% except in the immediate vicinity of the transition point.

VSL velocity profile data are compared with the TFD inviscid solution[24] and the turbulent BL solution[31] in Figure 10. In the outer predominantly inviscid portion of the shock layer, the VSL solution is in good agreement with the inviscid solution. The velocity profile data in the inner viscous region shows satisfactory agreement near the surface but large differences are obtained near the outer edge of the BL. The temperature profiles (see Figure 11) are in satisfactory agreement with maximum differences of less than ±10% in the viscous inner region and less than ±3% in the outer inviscid region.

The VSL solution was first obtained using the transport property data for hydrogen and helium presented by Lick and Emmons[32] and Esch, et al.[16] Using these transport properties, large differences between the VSL solution and that of Reference 31 were noted, and the transport property data were changed to conform with those used in the BL solution. The heating-rate distributions corresponding to the transport property data of References 16 and 32 are presented in Figure 12 for both radiating and nonradiating laminar and turbulent flows. The convective

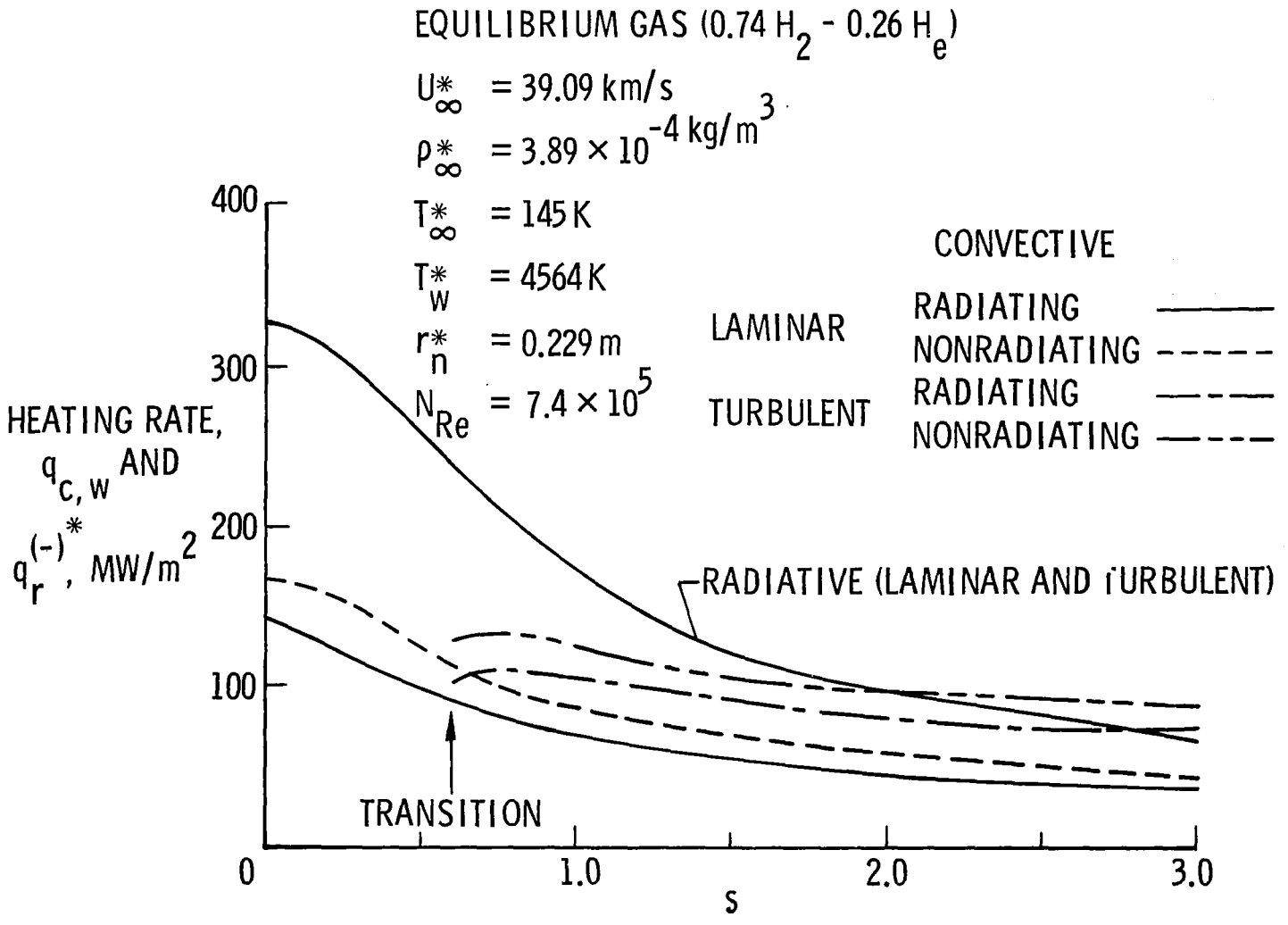

Figure 12. Heating-rate distributions for a 40° hyperboloid.

heating rates obtained with these transport properties are approximately 25% to 40% greater than those presented in Figure 9 for the nonradiating case. These two solutions for identical freestream conditions and body shape effectively demonstrate the difficulties to be expected when attempting to make comparisons of different analyses for equilibrium gas mixtures. For this problem, radiation heat transfer from the shock layer results in a reduction of temperature gradients in the viscous inner region with a corresponding reduction in convective heating rates at the surface for both laminar and turbulent flows. The radiation heat transfer to the surface is not significantly influenced by turbulence for this case.

3. DEVELOPMENT OF AN ADVANCED TURBULENCE MODEL

Results of the preceding section show that, using the mixing-length method, satisfactory solutions for viscous shock layers can be obtained provided the necessary boundary-layer parameters — boundary-layer thickness, displacement thickness, and edge conditions — are accurately defined. These boundary-layer parameters are needed for the mixing-length model, and are otherwise not essential to the solution of the VSL equations. As shown in Subsection 2.2, for nonradiating perfect gases and mixtures of perfect gases in chemical equilibrium, these parameters can be satisfactorily defined by assuming that the edge of the predominantly viscous layer is located at the point where the local total enthalpy is 99.5% of the freestream value. However, since energy is transferred out of the shock layer by radiation, this definition is unsuitable for radiating gas flows. The composite diffusion-conduction-dissipation index defined by Equation (25) provides a more suitable method for defining boundary-layer thickness, although the definition is adversely influenced by the nonvanishing normal gradient of the tangential velocity component in the nose region of blunt bodies. Hence, a turbulence modeling technique which is independent of the usual boundary-layer parameters is needed for VSL applications.

Recent progress in development of phenomenological turbulence-model equations for boundary layer applications indicate that these techniques can be appropriately modified for VSL applications. The most extensively developed and tested turbulence model of this class is that proposed by Saffman[33,34] and Wilcox.[35,36] The equations have been formulated for compressible flows,[34-36] and have been shown to be quite accurate in predicting freestream-turbulence-induced stagnation heating augmentation.[37] To achieve a solution, the model requires no

advance knowledge of a given turbulent flow aside from boundary and initial conditions. This fact, combined with the model's independence of boundary-layer parameters, illustrates the model's suitability for VSL applications.

In this study, preliminary steps have been taken to incorporate the model equations postulated by Wilcox and Traci[36] into the VSL code described in Section 2. The model equations are stated in Subsection 3.1. Then, in Subsection 3.2, boundary conditions suitable for surfaces with mass injection are developed. Model-predicted flow structure near the edge of the predominantly viscous region is then analyzed in Subsection 3.3. Finally, Subsection 3.4 proposes an algorithm for reducing computing times attending solution of the model equations.

3.1 THE MODEL EQUATIONS

The mean equations of motion, Equations (1) through (6), remain unaltered. The eddy viscosity, μ_T, is defined in terms of the turbulent mixing energy, e, and the turbulent dissipation rate, w, as follows:

$$\mu_T = \rho^2 e/w \tag{30}$$

In the Wilcox-Traci model, the mixing energy and dissipation rate satisfy the following nonlinear diffusion equations.

$$\rho\left(\frac{u}{1+n\kappa}\frac{\partial e}{\partial s} + v\frac{\partial e}{\partial n}\right) = \left[\alpha^*\rho\bar{S} - \beta^* w\right]e + \tilde{\sigma}^2\left\{\frac{\partial}{\partial n}\left[\mu(1+\sigma^*\varepsilon^+)\frac{\partial e}{\partial n}\right] + \left(\frac{\kappa}{1+n\kappa} + \frac{j\cos\theta}{r+n\cos\theta}\right)\mu(1+\sigma^*\varepsilon^+)\frac{\partial e}{\partial n}\right\} \tag{31}$$

$$\rho\left(\frac{u}{1+n\kappa}\frac{\partial w^2}{\partial s} + v\frac{\partial w^2}{\partial n}\right) = \left\{\alpha\rho\bar{S} - \left[\beta+2\sigma\left(\frac{\partial \ell}{\partial n}\right)^2\right]w\right\}w^2 + \tilde{\sigma}^2\left\{\frac{\partial}{\partial n}\left[\mu(1+\sigma\varepsilon^+)\frac{\partial w^2}{\partial n}\right] + \left(\frac{\kappa}{1+n\kappa} + \frac{j\cos\theta}{r+n\cos\theta}\right)\mu(1+\sigma\varepsilon^+)\frac{\partial w^2}{\partial n}\right\} \tag{32}$$

The quantities $\bar{S}$ and ℓ are given by the following:

$$\ell = \rho e^{1/2}/w \quad , \quad \bar{S} = \sqrt{S_{ij}S_{ji}} \tag{33}$$

where S_{ij} is the mean rate of strain tensor. There are six closure coefficients appearing in Equations (31) and (32), viz, $\alpha, \alpha^*, \beta, \beta^*, \sigma$, and σ^*. The following values have been established by arguments based on general properties of turbulent flows.[36]

$$\left.\begin{aligned} \beta &= \frac{3}{20} & \beta^* &= \frac{9}{100} \\ \sigma &= \frac{1}{2} & \sigma^* &= \frac{1}{2} \\ \alpha &= \frac{1}{3}\left[1 - \frac{10}{11}\exp\left(-\varepsilon^+/2\right)\right] \\ \alpha^* &= \frac{3}{10}\left[1 - \frac{10}{11}\exp\left(-2\varepsilon^+\right)\right] \end{aligned}\right\} \tag{34}$$

3.2 SURFACE BOUNDARY CONDITIONS

At solid boundaries with no mass addition, Saffman and Wilcox[34] have shown that in addition to the no-slip velocity and surface-temperature (or heat transfer) boundary conditions, the following boundary conditions must be imposed on e and w:

$$e = 0 \quad , \quad w = \frac{\rho_w^2 u_\tau^2}{\mu_w \alpha_\infty^*} S_R(k^+) \quad \text{at} \quad n = 0 \tag{35}$$

where S_R is a universal function of the roughness height of the surface, k, and

$$k^+ \equiv \rho_w u_\tau k/\mu_w$$

The constant α_∞^* is 3/10, the high-Reynolds-number ($\varepsilon^+ >> 1$) value of α^*. For boundary layers with surface mass injection

(blowing), the introduction of an additional velocity scale (v_w = normal flow velocity at the surface) suggests that some modification of Equation (35) may be required for flows with blowing. Andersen, et al,[38] provide further evidence that the dissipation-rate boundary condition must be revised when blowing is present by showing, from correlation of their experimental data, that the law of the wall assumes the following modified form:

$$\frac{u}{u_\tau} = \frac{1}{\tilde{k}_1} \log \frac{u_\tau y}{\nu} + \tilde{C} \tag{36}$$

The modified "constants" $\tilde{k}_1$ and $\tilde{C}$ are related to k_1, C, and the blowing velocity as follows:

$$\left.\begin{aligned} \tilde{k}_1 &= k_1/(1 + 7.7\ v_w^+) \\ \tilde{C} &= C - 50\ v_w^+ + 72(v_w^+)^2 \end{aligned}\right\} \tag{37}$$

Since Saffman and Wilcox's computations show that C is strongly affected by the value of S_R, Andersen's data indicate that a modification to the model equation boundary condition is required for computing blown boundary layers. Since mass injection is of key importance in VSL applications, we thus consider effects of blowing on model-predicted flow structure.

As in the case of rough surfaces, we can establish suitable boundary conditions for flows with mass injection by analyzing the viscous sublayer of an incompressible plane-wall boundary layer. Denoting distance normal to the surface by y, the blown sublayer equations are

$$\nu(1+\varepsilon^+)\frac{du}{dy} = u_\tau^2 + v_w u \tag{38}$$

$$v_w \frac{de}{dy} = \left\{\alpha^* \left|\frac{du}{dy}\right| - \beta^* \frac{w}{\rho}\right\} e + \frac{d}{dy}\left[\nu(1+\sigma^*\varepsilon^+)\frac{de}{dy}\right] \tag{39}$$

$$v_w \frac{dw^2}{dy} = \left\{ \alpha \left| \frac{du}{dy} \right| - \left[\beta + 2\sigma \left(\frac{d\ell}{dy} \right)^2 \right] \frac{w}{\rho} \right\} w^2 + \frac{d}{dy} \left[\nu (1+\sigma\varepsilon^+) \frac{dw^2}{dy} \right] \qquad (40)$$

where ν is kinematic viscosity.

To establish boundary conditions for this fifth-order system, we assume the effluent gas is free of turbulent fluctuations so that e vanishes at the surface. The horizontal velocity, u, vanishes by virtue of the no-slip condition, and in analogy to Equations (35) we write

$$u = e = 0 \quad , \quad w = \frac{\rho u_\tau^2}{\alpha_\infty^* \nu} S_B (v_w^+) \quad \text{at} \quad u_\tau y/\nu = 0 \qquad (41)$$

where S_B is a universal function of v_w^+. Examination of wall-layer structure (i.e., the asymptotic solution for $u_\tau y/\nu \to \infty$) predicted by Equations (38-40) yields two more boundary conditions valid as $u_\tau y/\nu \to \infty$. As can be easily shown, the turbulent diffusion term in the mixing-energy equation is negligible for $u_\tau y/\nu \to \infty$, and there follows

$$e \to \frac{u_\tau^2}{\alpha_\infty^*} \left[1 + v_w^+ \frac{u}{u_\tau} \right] , \quad w \to \frac{\rho}{\alpha_\infty^*} \frac{du}{dy} \quad \text{as} \quad u_\tau y/\nu \to \infty \qquad (42)$$

In addition to establishing boundary conditions, further examination of the wall-layer solution demonstrates direct correspondence between model-predicted and measured effects of blowing on a turbulent boundary layer. Specifically, in the limit of weak blowing ($v_w^+ << 1$), expanding in powers of v_w^+ shows that the velocity obeys a modified law of the wall similar to Equation (36). The effective Karman constant is predicted to be

$$\tilde{k}_1 = k_1/(1 + \Xi v_w^+) \qquad (43)$$

where

$$\Xi = \frac{4k_1 C - 1}{8k_1} + \frac{1}{4k_1} \log \frac{u_\tau y}{\nu} \qquad (44)$$

The functional dependence in Equation (43) is similar to that quoted by Andersen [Equation (37)]. Table 1 shows the variation of Ξ with $u_\tau y/\nu$ for $k_1 = 0.41$ and $C = 5.5$. As shown, the predicted value of Ξ is reasonably close to Andersen's value of 7.7, particularly at the larger values of $u_\tau y/\nu$.

Table 1. Variation of Ξ with $u_\tau y/\nu$.

$u_\tau y/\nu$	Ξ
10	3.84
100	5.25
500	6.23
1000	6.65

Using an implicit, time-marching numerical method, sublayer calculations were performed for several blowing rates ranging from $v_w^+ = 0$ to $v_w^+ = 0.7393$. The value of S_B was varied for each blowing rate until close agreement with the velocity profile data of Andersen, et al,[38] was obtained (Figure 13). As expected from the wall-layer analysis, slopes of the various profiles (i.e., $\tilde{k}_1^{-1}$) are accurately predicted. Note that this means that, similar to the case of surface roughness, the dissipation-rate boundary condition primarily determines the variation of $\tilde{C}$ with v_w^+. Figure 14 presents a correlation of S_B with v_w^+; an accurate analytical representation of the correlation is

$$S_B = \frac{6}{v_w^+(1+v_w^+)} \quad ; \quad v_w^+ > 0 \qquad (45)$$

Although effects of suction ($v_w^+ < 0$) have not been considered here, computations performed by Wilcox[39] imply that w is unaffected by suction. Therefore, Equation (45) should only be used for $v_w^+ > 0$.

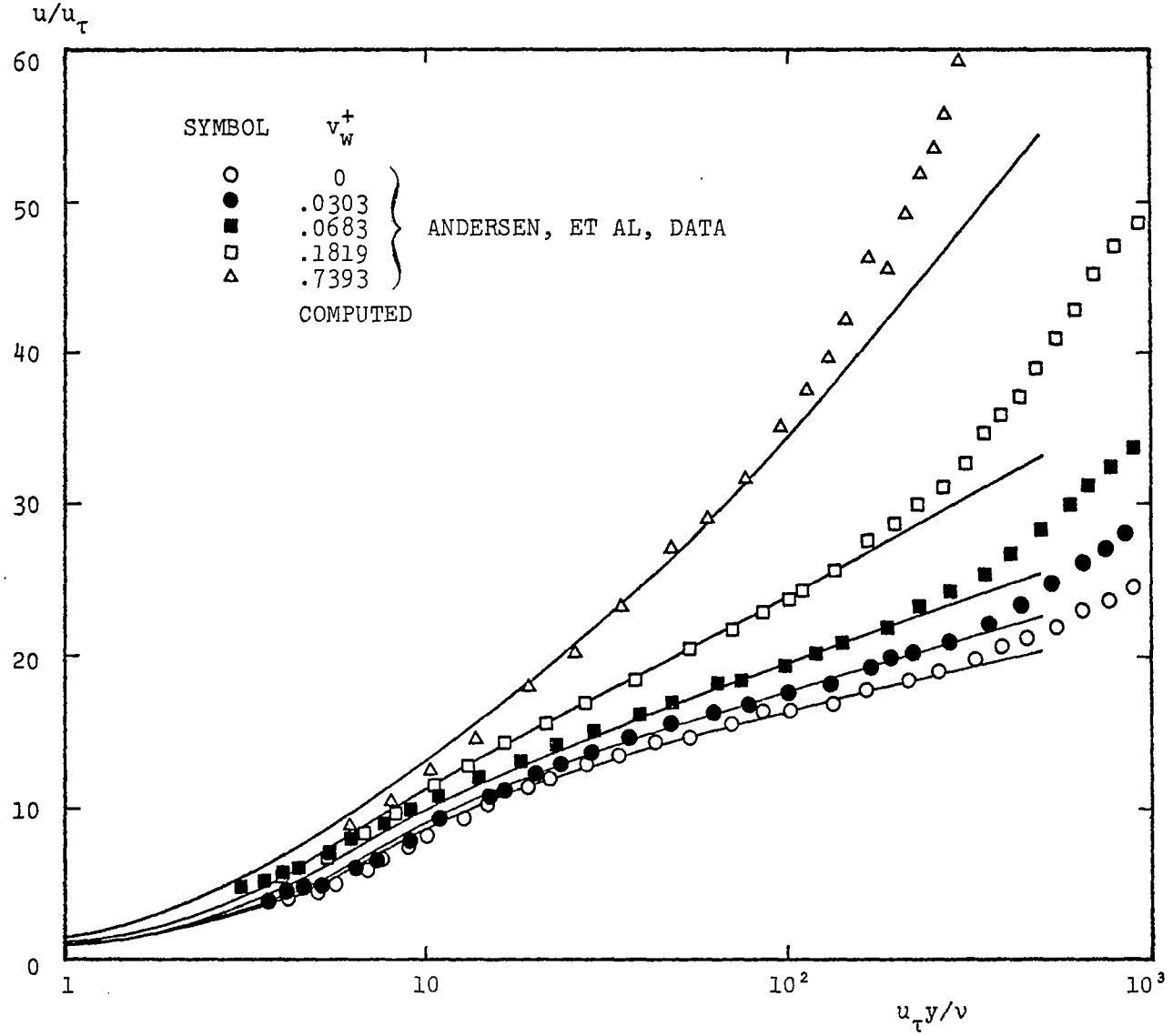

Figure 13. Comparison of computed and measured sublayer velocity profiles for boundary layers with surface mass injection.

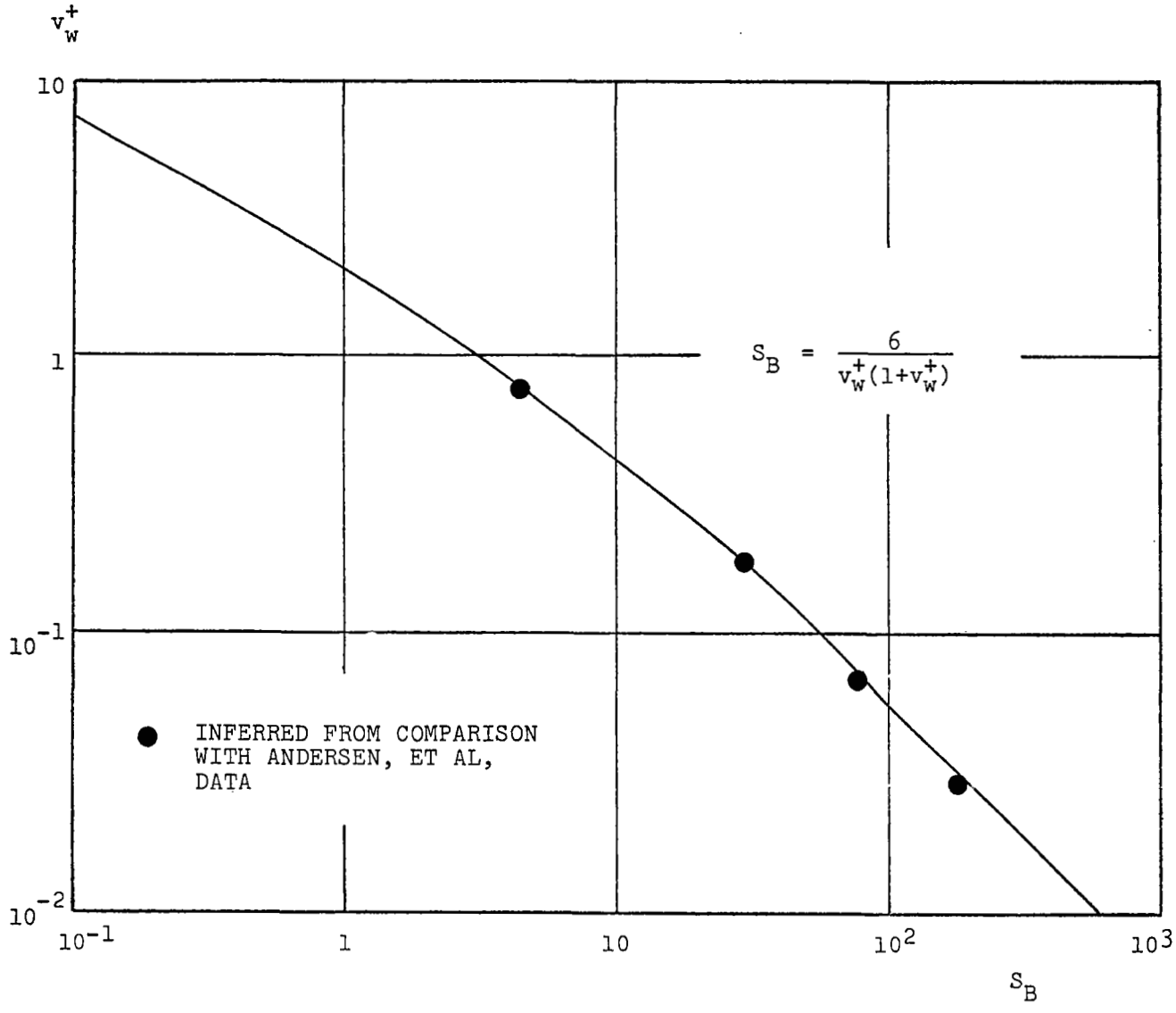

Figure 14. Correlation of S_B with blowing rate parameter, v_w^+.

3.3 TURBULENT-NONTURBULENT INTERFACE STRUCTURE

We now consider model-predicted flow structure near the outer edge of the predominantly viscous region. In solving the model equations, numerical difficulties have been encountered near the outer edge both in conventional boundary-layer computations and in preliminary VSL applications. The difficulties stem from existence of a sharp turbulent-nonturbulent interface at the boundary-layer edge. The sharpness, first analyzed by Saffman,[33] manifests itself as discontinuities in $\partial u^*/\partial y$ and $\partial w/\partial y$. Accurate numerical solutions require accounting for these discontinuities; therefore, we review interface structure and propose a tentative remedy in this section.

3.3.1 Interface Structure for a Conventional Boundary Layer

As can be easily verified for the special case $e = w = 0$ in the freestream, production and dissipation terms [i.e., the first terms in brackets on the right-hand sides of Equations (31) and (32)] and molecular diffusion are negligible near the interface; approaching the interface from below, the asymptotic behavior of e, w, and u* is

$$\left.\begin{aligned} e &\sim (\delta-y)^2 \\ w &\sim (\delta-y) \\ u^* &\sim (\delta-y) \end{aligned}\right\} \quad \text{as } y \to \delta^- \tag{46}$$

where δ is boundary layer thickness. Note that the behavior predicted in Equation (46) is consistent with experimental observations. Specifically, Nee and Kovasznay[40] have observed that the mean velocity varies linearly with distance from the interface, i.e., $u^* \sim (\delta-y)$. Also, the length scale has been observed by many experimenters to approach a nonzero value near the edge of a turbulent flow which implies $\ell \sim \rho e^{\frac{1}{2}}/w \sim$ constant as $y \to \delta$.

Of course such discontinuities cannot exist in a truly viscous flow. As shown by Saffman[33] and by Wilcox and Traci,[36] there is a thin region centered at the boundary layer edge in which viscous effects become important. This region is known as the viscous superlayer; its role is to remove the discontinuities in $\partial u^*/\partial y$ and $\partial w/\partial y$. Superlayer thickness is proportional to ν^*/v_e^* where v_e^* is entrainment velocity. Although v_e^* is generally very small for a conventional boundary layer, resolving the superlayer is impractical in a numerical computation. Consequently, solutions to the equations appear to be discontinuities even in a viscous computation.

In prior boundary layer computations, we have used the known algebraic behavior of e, w, and u* to locate the boundary-layer edge and to obviate numerical difficulties attending the solution "discontinuities"; the procedure is as follows. First, the equations of motion are integrated to a point thought to be beyond $y = \delta$. The solution is then examined to determine the value of y at which any one (or more) of the three quantities e, w, or u* is less than its boundary-layer-edge value. The interface discontinuities always cause such undershooting, and the dissipation rate is usually the first quantity to undershoot its edge value. If no such undershoot occurs, the equations are integrated to a larger value of y. Ultimately, the boundary-layer edge is located by linear extrapolation, from points below the undershoot location, of the computed values of either u* or w. For classical boundary layers, this procedure obviates numerical difficulties attending insufficient resolution of the superlayer; however, the procedure's applicability for VSL's is uncertain. In fact, a key advantage of using the model equations, i.e., independence of boundary layer thicknesses, is lost if this procedure is used. In the following sections we analyze interface structure for stagnation point flow and postulate an alternative procedure.

3.3.2 Interface Structure for Stagnation Point Flow

To determine similarities between interface structure for VSL's and conventional boundary layers, we now analyze flow near a stagnation point (Figure 15). This flow is relevant because a VSL begins at a stagnation point and approaches a conventional boundary layer farther downstream. For perfect-gas flow near the stagnation point of a bluff body, the equations of motion admit a similarity solution;[37] the similarity variables are

$$\xi = \sqrt{\frac{c^*}{\nu_\infty^*}}\, x$$
$$\eta = \sqrt{\frac{c^*}{\nu_\infty^*}}\, y \qquad (47)$$

The quantity c^* is the inviscid flow velocity gradient which depends on the shape of the body and the Mach number. Provided the shock standoff distance is large compared to the thickness of the viscous region, the mean flow outside the viscous region ($y > \delta$) satisfies the usual inviscid solution near a stagnation point given by

$$u^* = c^* x \quad , \quad v^* = -(j+1)c^* y \qquad (48)$$

where $j=0$ for two-dimensional flow and $j=1$ for axisymmetric flow. The various dependent variables are scaled as follows:

$$\left.\begin{aligned} u^* &= \nu_\infty^* c^* \xi\, U(\eta) \\ v^* &= \nu_\infty^* c^*\, V(\eta) \\ T^* &= T_\infty T(\eta) \\ e &= \nu_\infty^* c^*\, E(\eta) \\ w &= \rho_\infty^* c^*\, W(\eta) \end{aligned}\right\} \qquad (49)$$

The transformed equations of motion are

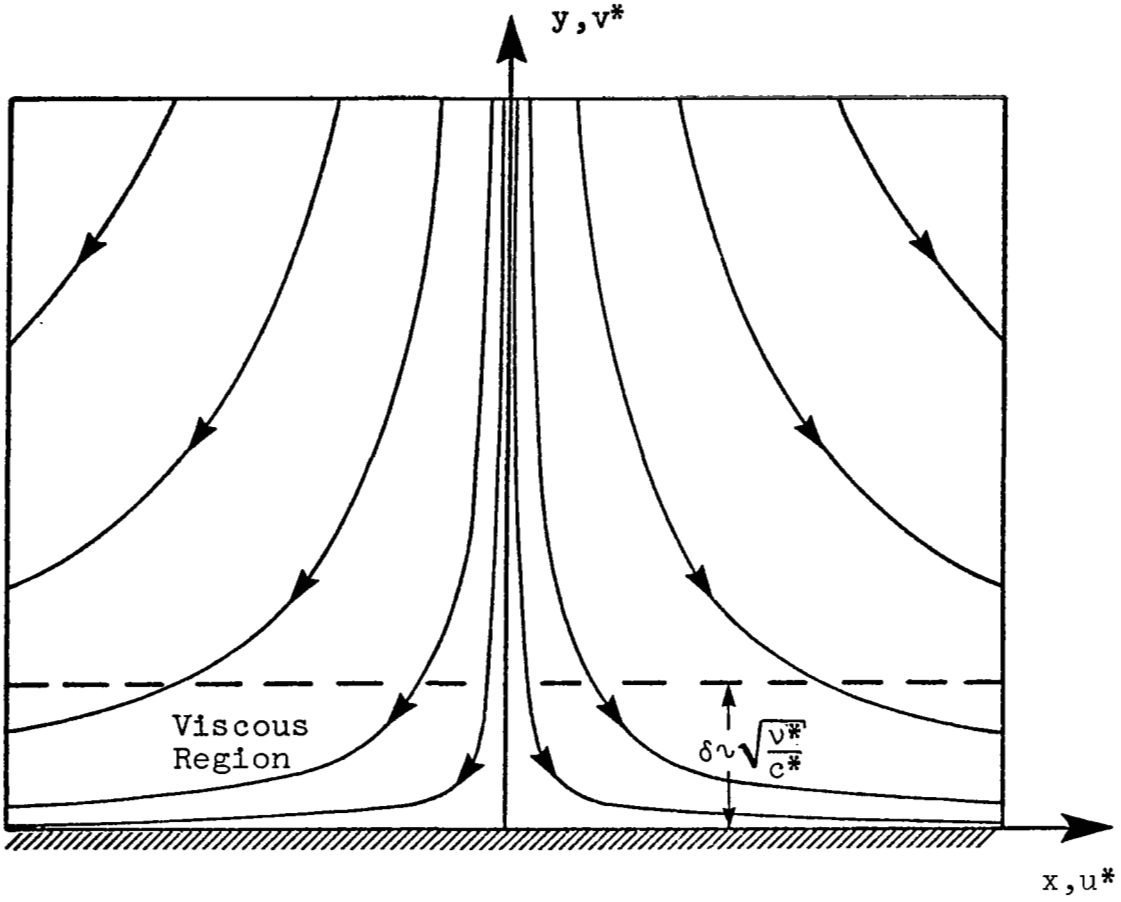

Figure 15. Schematic of stagnation point flowfield.

Mass Conservation

$$\frac{dV}{d\eta} + (j+1)U = 0 \tag{50}$$

Horizontal Momentum Conservation

$$V\frac{dU}{d\eta} = 1 - U^2 + \frac{d}{d\eta}\left[(1+\varepsilon^+)\frac{dU}{d\eta}\right] \tag{51}$$

Energy Conservation

$$V\frac{dT}{d\eta} = \frac{d}{d\eta}\left[\left(\frac{1}{N_{Pr}} + \frac{\varepsilon^+}{N_{Pr,T}}\right)\frac{dT}{d\eta}\right] \tag{52}$$

Turbulent Mixing Energy

$$V\frac{dE}{d\eta} = \left\{2\alpha^*\sqrt{2j+1}\,|U| - \beta^* W\right\}E + \frac{d}{d\eta}\left[(1+\sigma^*\varepsilon^+)\frac{dE}{d\eta}\right] \tag{53}$$

Turbulent Dissipation Rate

$$V\frac{dW^2}{d\eta} = \left\{2\alpha\sqrt{2j+1}\,|U| - \beta W - 2\sigma W\left(\frac{dL}{d\eta}\right)^2\right\}W^2 + \frac{d}{d\eta}\left[(1+\sigma\varepsilon^+)\frac{dW^2}{d\eta}\right] \tag{54}$$

where L and ε^+ are defined as

$$\left.\begin{aligned} L &= E^{\frac{1}{2}}/W \\ \varepsilon^+ &= E/W \end{aligned}\right\} \tag{55}$$

Equations (50)-(55) constitute a 9th order set of coupled ordinary differential equations. For a perfectly smooth wall with no mass injection, the boundary conditions are

$$\left.\begin{aligned} U(0) &= E(0) = V(0) = 0 \\ T(0) &= T_W^*/T_\infty^* \\ W(\eta) &\to \frac{20}{\beta}\eta^{-2} \quad \text{as} \quad \eta \to 0 \end{aligned}\right\} \tag{56}$$

while (denoting $Re_D = \rho_\infty^* U_\infty^* D_\infty^* / \mu_\infty^*$ where D* is body diameter)

$$\left.\begin{aligned} U(\eta) &\to 1 \ , \ T(\eta) \to 1 \\ E(\eta) &\to Re_D (e_\infty / U_\infty^2)(U_\infty / cD) \\ W(\eta) &\to \frac{\sqrt{e_\infty / U_\infty^2}}{\ell_\infty / D} (U_\infty / cD) \end{aligned}\right\} \quad \text{as} \quad \eta \to \infty \tag{57}$$

Unlike the conventional boundary layer, the production rates in Equations (53) and (54), i.e., $2\alpha^*\sqrt{2j+1}\,|U|$ and $2\alpha\sqrt{2j+1}\,|U|$, are nonvanishing above the viscous region. As a consequence, there is apparently no sharpness at the turbulent-nonturbulent interface. For example, Figures 16-18 show computed e, ℓ, and ε^+ profiles (i.e., the curves labeled "without intermittency") for a case in which both e and w are very small outside the viscous region ($y/\sqrt{\nu^*/c^*} \lesssim 6$); computations have been performed with the same implicit, time-marching method used in the sublayer computations of Subsection 3.2. All three quantities smoothly approach their freestream values. Thus, the numerical difficulties present in our early VSL computations are not associated with flow in the immediate vicinity of the stagnation point. Rather, these difficulties must be caused by appearance of the sharp interface as the VSL approaches conventional boundary-layer structure.

3.3.3 Tentative Modification to the Model Equations

Having identified the source of difficulty as the sharp interface, we now propose a tentative remedy. Inspection of Equations (31) and (32) shows that, unlike the basic conservation equations, we can never obtain solutions for which e and w simultaneously approach constant, nonvanishing values. To understand this, note that vanishing of the source term in either equation precludes vanishing of the other equation's source term. As shown by Wilcox and Traci,[36], the source terms play a secondary role right at the interface. Nevertheless, the stagnation-point analysis above

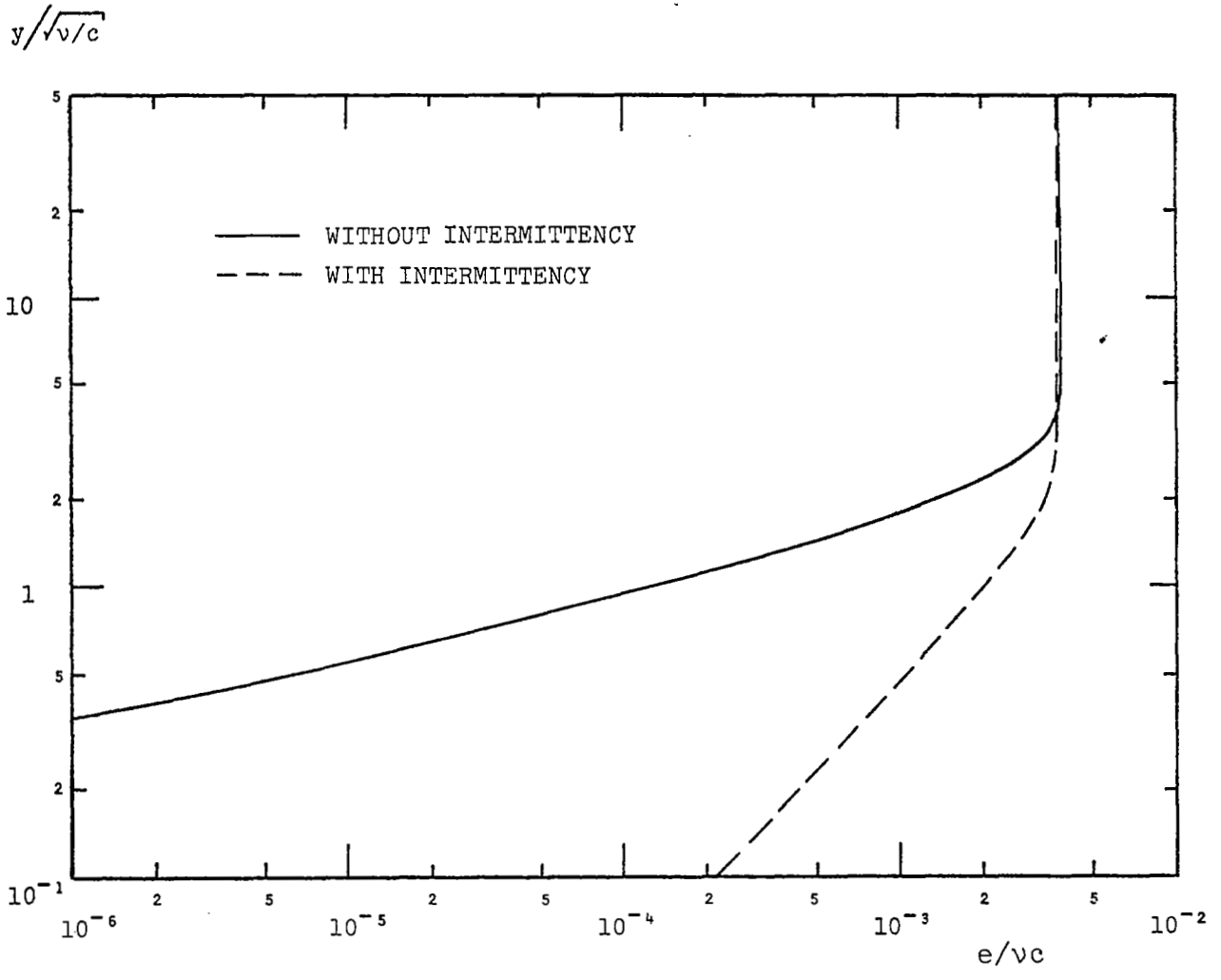

Figure 16. Computed variation of turbulent mixing energy near a stagnation point.

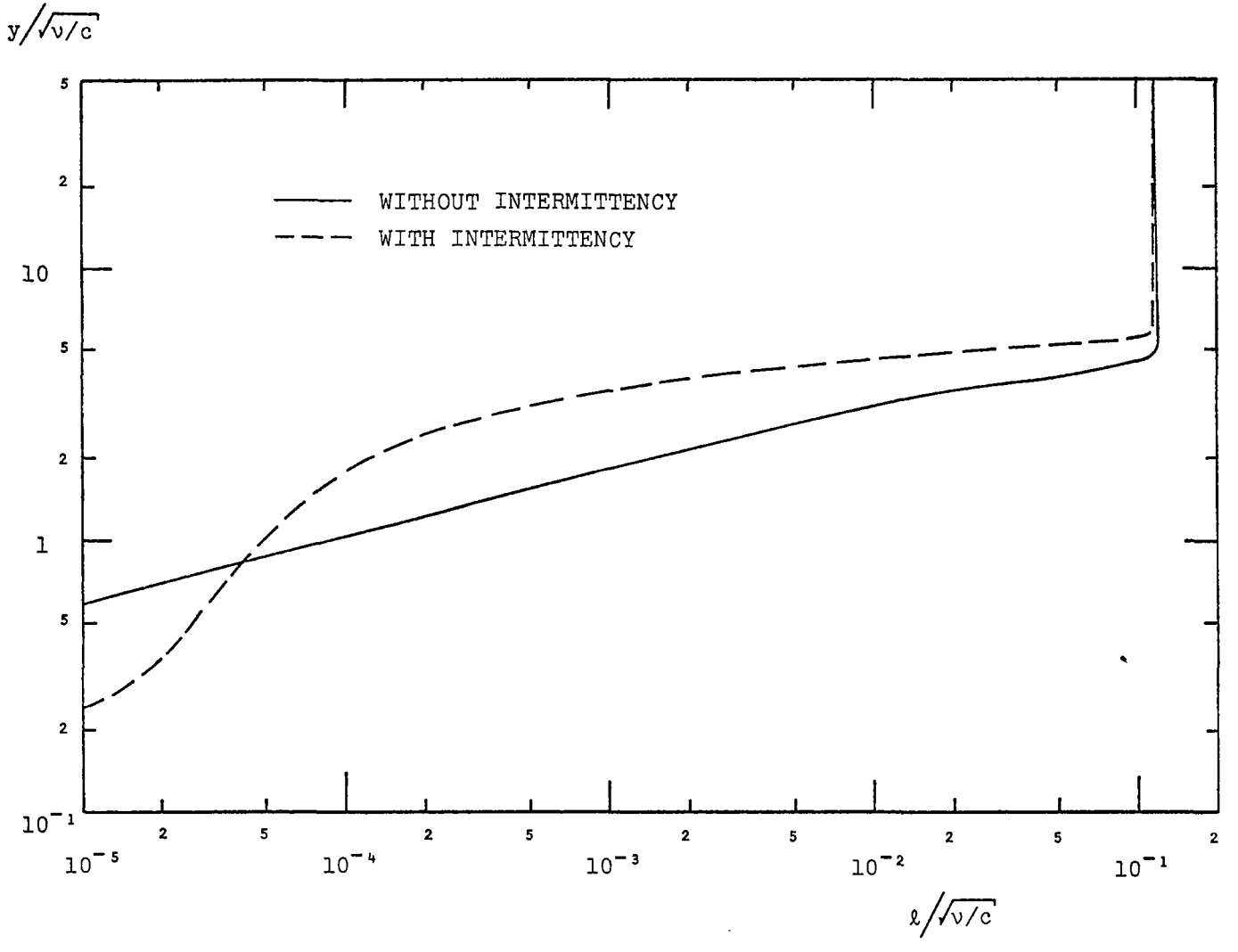

Figure 17. Computed variation of turbulent length scale near a stagnation point.

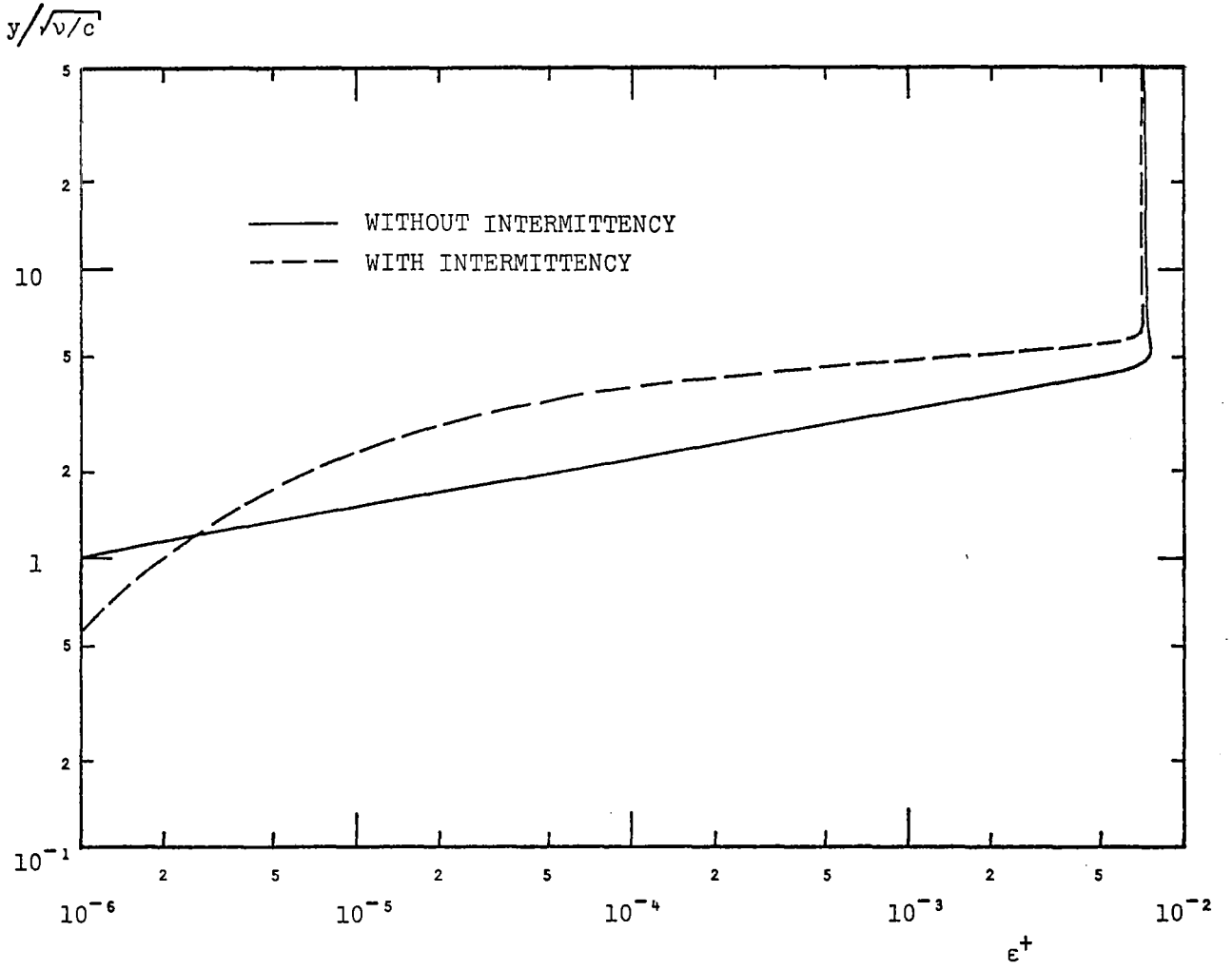

Figure 18. Computed variation of eddy viscosity near a stagnation point.

shows that alterations to the source terms give rise to significant modification to interface structure.

As a numerical experiment and a potential remedy for the numerical difficulties encountered in VSL computations with the model equations, we propose forcing the source terms in Equations (31) and (32) to vanish outside the predominantly viscous region. To accomplish this end, we in effect introduce intermittency factors, I_e and I_w, which multiply the source terms, i.e.

$$[\alpha^*\rho\bar{S} - \beta^* w]e \rightarrow I_e[\alpha^*\rho\bar{S} - \beta^* w]e \tag{58}$$

$$\left\{\alpha\rho\bar{S} - \left[\beta + 2\sigma\left(\frac{\partial \ell}{\partial n}\right)^2\right]w\right\}w^2 \rightarrow I_w\left\{\alpha\rho\bar{S} - \left[\beta + 2\sigma\left(\frac{\partial \ell}{\partial n}\right)^2\right]w\right\}w^2 \tag{59}$$

A VSL computation was performed with

$$I_e = I_w = \tau/\tau_w \tag{60}$$

where τ is Reynolds shear stress. No numerical difficulties were encountered, thus verifying that the nonvanishing of the source terms above the viscous layer is the primary source of difficulty.

In order to achieve a more universal (tensor invariant) formulation, an alternate definition for I_e and I_w must be proposed. One possibility follows from noting that $\partial \ell/\partial n$ vanishes above both conventional boundary layers and above the viscous region in VSL's. Thus, we propose the following

$$I_e = I_w = 1 - \exp\left[-\Gamma\left(\frac{\partial \ell}{\partial n}\right)^2\right] \tag{61}$$

To assess the effect of the intermittency modifications on predicted stagnation-point flow properties, the computations

discussed in Subsection 3.2.2 were repeated using the intermittency defined in Equation (61) with $\Gamma = 50$. Figures 16-18 show that the solution is strongly affected by intermittency throughout the flow, including deep in the viscous region. Because the eddy viscosity is so small, the mean velocity profile is unaffected. However, the intermittency modification conceivably has a nontrivial effect on velocity profiles in regions where the flow is fully turbulent. Additionally, the model's ability to predict transition[39] may be affected by damping the source terms. Hence, the intermittency modification must be viewed as tentative until the impact of the modification upon these and other important aspects of model-predicted flow properties have been quantified.

3.4 COMPUTING-TIME REDUCTION

Even with the intermittency modification, computing times with the VSL program are excessive when the model equations are used. The maximum streamwise step size at which converged solutions can be obtained is less than a tenth of that which can be used in mixing-length computations. In order to reduce computing time, a special integration algorithm has been devised. In this section, we discuss the reason for the reduced step size and present the integration algorithm.

Step size must be reduced with the model equations because the source terms are very large and negative close to a solid boundary. Consequently, in a boundary-layer marching procedure, there is a tendency to overestimate the decay of numerical errors from one station to the next (Figure 19). Unless very small steps are taken as we march from $x = x_1$ to $x = x_2$, the magnitude of a numerical error, δe, can grow very rapidly and ultimately can destroy the solution. By taking smaller steps, we more nearly approach the rapid exponential decay implied by the large and negative source terms, thus preserving solution accuracy.

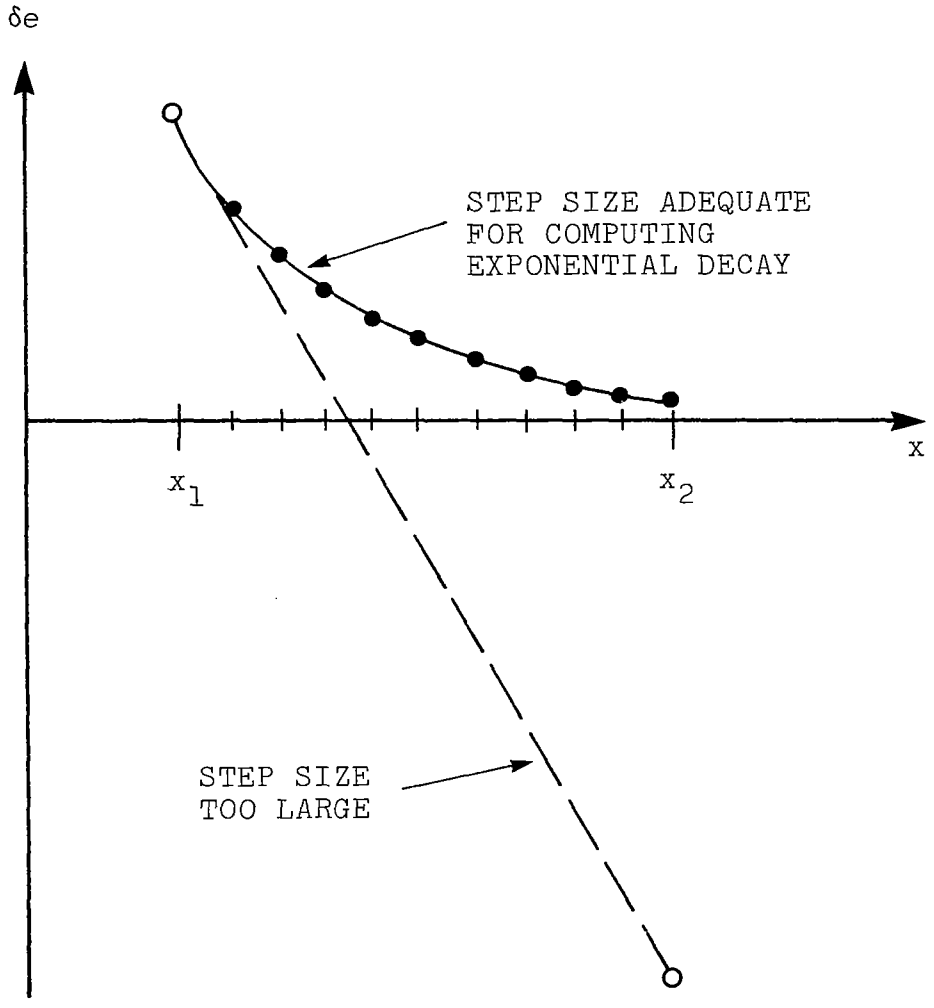

Figure 19. Schematic illustrating error growth in a numerical computation.

Above the viscous sublayer the source terms are generally much smaller. Hence, it may be necessary to take small steps in the streamwise direction only in the sublayer while much larger steps may be permissible elsewhere. To test this possibility, two incompressible flat-plate boundary layer computations were made with a second-order-accurate, implicit boundary-layer code. In the computations, we solved the conservation equations only at every n^{th} streamwise station. At each n^{th} station, the conservation equations were solved all the way across the boundary layer. Below a specified distance normal to the surface, $y_{j_{max}}$, the model equations were solved at every streamwise station. In addition, the model equations were solved all the way across the boundary layer at each n^{th} station.

The first round of computations was for a fully turbulent boundary layer; the computation used 100 mesh points between $y = 0$ and $y = \delta$ while the value of n was 8. Figure 20 shows the ratio of computing times, t/t_o, for three values of j_{max}: t is the computing time required when $n = 8$ and t_o is the computing time required for a normal boundary layer computation, i.e., $n = 1$ and $j_{max} = 100$. As shown, there is a 17% reduction in computing time when the model equations are solved up to $y = \delta$, i.e., for $j_{max} = 100$. However, when j_{max} is 30, computing time is nearly halved. Further reduction of j_{max} results in a slight increase in computing time; this increase is caused by an attendant increase in the number of iterations required to obtain a converged solution. In all computations we observed no deterioration in solution accuracy.

The second round of computations was for a laminar/transitional boundary layer; starting from the plate leading edge, the equations of motion were integrated up to the model-predicted transition point at a plate-length Reynolds number, Re_x, of

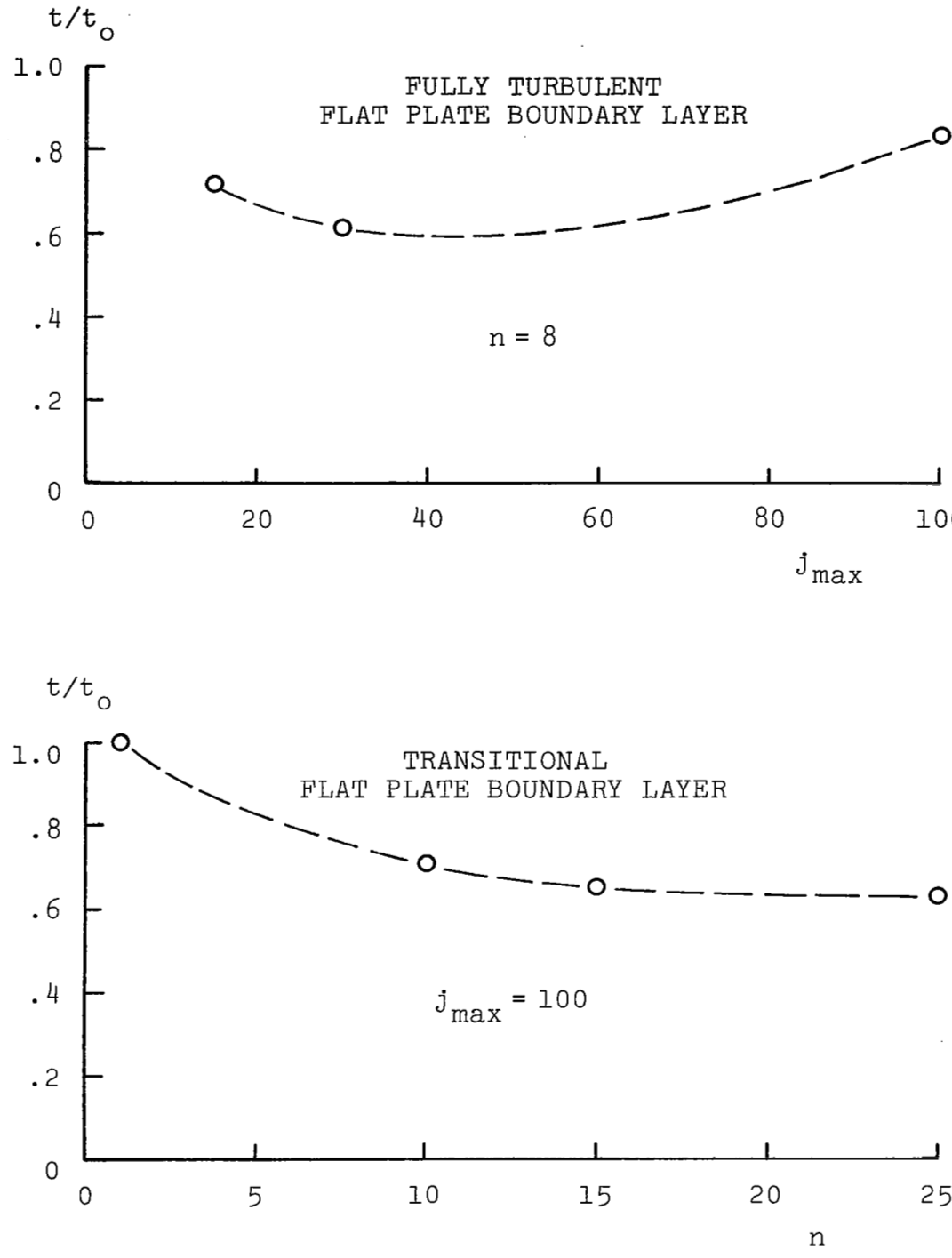

Figure 20. Computing time reduction attending the special integration algorithm.

$2.1 \cdot 10^6$. Using $j_{max} = 100$, we varied n from 1 to 25. As shown in Figure 20, t/t_o drops by 30% as n increases to 10; a slower decrease in t/t_o follows as n increases further with a large n asymptote of $t/t_o \doteq 0.60$. Varying n causes no variation in transition Reynolds number.

This new integration algorithm, in effect, permits an order of magnitude increase in streamwise step size. The reduction in computing time is somewhat disappointing however. A significant increase in the number of iterations required to achieve converged solutions prevents computing time from decreasing proportionally with j_{max} and/or n. Nevertheless, the computations verify the proposed cause of step size reduction, viz, the large and negative source terms in the model equations, particularly near a solid boundary. Having attained such understanding, we are now in a position to develop even more efficient integration algorithms.

4. CONCLUDING REMARKS

As shown in Section 2, numerical solutions for the viscous-shock-layer equations compare favorably with inviscid flowfield solutions in the inviscid outer portion of the shock layer. Favorable comparisons with boundary-layer solutions are obtained for the predominantly viscous inner portion of the shock layer both near the nose and far downstream where vorticity interaction is negligible. In flow regions where vorticity interaction is strong, the viscous-shock-layer solutions appear to be more satisfactory.

First-order boundary-layer theory with corrections for streamline swallowing appear to overpredict boundary-layer and displacement thicknesses. For turbulent flow, this results in an apparent overprediction of skin friction and heat transfer if vorticity interaction is strong. This behavior is the result of the implied nonvanishing normal gradients at the edge of the boundary layer when longitudinal entropy gradients are considered.

Experimental data are needed for hypersonic turbulent flows over blunt bodies to assess the accuracy of the present numerical solution procedure and to determine the validity of mixing-length turbulence models in the presence of strong vorticity interaction.

Turbulence models that are independent of conventional boundary-layer thickness parameters are needed for both the present method of analysis and for numerical solution of the Navier-Stokes equations. The analyses of Section 3 demonstrate the potential of two-equation turbulence models in the VSL context. While further development of the model and methods for efficiently integrating the model equations will be needed to achieve a practical engineering design tool, the results are very encouraging.

REFERENCES

1. Moss, J.N., Anderson, E.C., and Bolz, C.W., Jr., "Viscous-Shock-Layer Solutions with Radiation and Ablation Injection for Jovian Entry," AIAA Paper No. 75-671, AIAA 10th Thermophysics Conference, Denver, Colorado (May 1975).

2. Davis, R.T., "Numerical Solution of the Hypersonic Viscous Shock-Layer Equations," AIAA J 8, No 5, pp 843-851 (1970).

3. Davis, R.T., "Hypersonic Flow of a Chemically Reacting Binary Mixture Past a Blunt Body," AIAA Paper No 70-805, (June-July 1970).

4. Moss, J.N., "Reacting Viscous-Shock-Layer Solutions with Multicomponent Diffusion and Mass Injection," NASA TR-411 (1974).

5. Moss, J.N., "Stagnation and Downstream Viscous-Shock-Layer Solutions with Radiation and Coupled Ablation Injection," AIAA Paper No 74-73, AIAA 12th Aerospace Science Meeting, Washington, D.C. (Jan 1974).

6. Eaton, R.R., and Larson, D.E., "Laminar and Turbulent Viscous Shock Layer Flow in the Symmetry Planes of Bodies at Angle of Attack," AIAA Paper No 74-599 (June 1974).

7. Anderson, E.C., and Moss, J.N., "Numerical Solution of the Viscous-Shock-Layer Equations for Hypersonic Turbulent Flow of a Perfect Gas About Blunt Axially Symmetric Bodies," NASA TN D-7865, 1975.

8. Anderson, E.C., and Moss, J.N., "Viscous-Shock-Layer Solutions for Turbulent Flow of Radiating Gas Mixtures in Chemical Equilibrium," NASA TM X-72764 (1975).

9. Bird, R.B., Stewart, W.E., and Lightfoot, E.N., Transport Phenomena, John Wiley & Sons, Inc (1960).

10. Dorrance, W.H., Viscous Hypersonic Flow, McGraw-Hill (1962).

11. Nicolet, W.E., "Advanced Methods for Calculating Radiation Transport in Ablation-Product Contaminated Boundary Layers," NASA CR-1656 (1970).

12. Nicolet, W.E., "User's Manual for the Generalized Radiation Transfer Code (RAD/EQUIL)," NASA CR-116353 (1969).

13. Stroud, C.W., and Brinkley, K.L., "Chemical Equilibrium of Ablation Materials Including Condensed Species," NASA TN D-5391 (1969).

14. Esch, D.D., Siripong, A., and Pike, R.W., "Thermodynamic Properties in Polynomial Form for Carbon, Hydrogen, Nitrogen, and Oxygen Systems from 300 to 15000° K," NASA CR-111989 (1970).

15. McBride, B.J., Heimel, S., Ehlers, J.G., and Gordon, S., "Thermodynamic Properties to 6000 K for 210 Substances Involving the First 18 Elements," NASA SP-3001 (1963).

16. Esch, D.D., Pike, R.W., Engel, C.D., Farmer, R.C., and Balhoff, J.F., "Stagnation Region Heating of a Phenolic-Nylon Ablator During Return from Planetary Missions," NASA CR-112026 (1971).

17. Wilke, C.R., "A Viscosity Equation for Gas Mixtures," Chem Phys J 18, No 4, pp 517-519 (1950).

18. Clauser, F.H., "The Turbulent Boundary Layer," Advances in Applied Mathematics, Vol IV, pp 1-51, Academic Press (1956).

19. Klebanoff, P.S., "Characteristics of Turbulence in a Boundary Layer with Zero Pressure Gradient, NACA 1247 (1955).

20. Cebeci, T., "Behavior of Turbulent Flow near a Porous Wall with Pressure Gradient," AIAA J 8, No 12, pp 2152-2156 (1970).

21. Van Driest, E.R., "On Turbulent Flow Near a Wall," Aero Sci J 23, No 11, pp 1007-1011, 1036 (1956).

22. Harris, J.E., "Numerical Solutions of the Equations for Compressible Laminar, Transitional, and Turbulent Boundary Layers and Comparisons with Experimental Data," NASA TR R-368 (1971).

23. Inouye, M., Rakich, J., and Lomax, H., "A Description of Numerical Methods and Computer Programs for Two-Dimensional and Axisymmetric Supersonic Flow over Blunt Nosed and Flared Bodies," NASA TN D-2970 (1965).

24. Sutton, K., "Coupled Nongray Radiating Flow About Planetary Entry Bodies," AIAA J 12, No 8, pp 1099-1105 (1974).

25. Anderson, E.C., and Lewis, C.H., "Laminar or Turbulent Boundary-Layer Flows of Perfect Gases or Reacting Gas Mixtures in Chemical Equilibrium," NASA CR-1893 (1971).

26. Mayne, A.W., Jr., and Dyer, D.F., "Comparison of Theory and Experiment for Turbulent Boundary Layers on Simple Shapes at Hypersonic Conditions," Proc of 1970 Heat Transfer and Fluid Mech Inst, Stanford Univ Press, pp 168-188 (1970).

27. Blottner, F.G., "Finite Difference Methods of Solution of the Boundary-Layer Equations," AIAA J 8, No 2, pp 193-205 (1970).

28. Price, S.M., and Harris, J.E., "Computer Program for Solving Compressible Nonsimilar Boundary-Layer Equations for Laminar, Transitional, or Turbulent Flows of a Perfect Gas," NASA TM X-2458 (1972).

29. Van Dyke, M., "A Review and Extension of Second-Order Hypersonic Boundary-Layer Theory," Rarefied Gas Dynamics, Fluid Symposium Supp 2, Vol II, Academic Press (1963).

30. Edquist, C.T., "A Technique for Predicting Shock Induced Vorticity Effects During Venus Entry," Martin-Marietta (Denver) R-70-48671-006 (1970).

31. Bartlett, E.P., and Kendall, R.M., "Nonsimilar Solution of the Multi-component Laminar Boundary Layer by an Integral Matrix Method," Aerotherm Corp (Palo Alto, CA) Rept No 66-7, Pt III (1967).

32. Lick, W.J., and Emmons, H.W., "Transport Properties for Helium from 200 to 50,000° K," Harvard Univ Press (1965).

33. Saffman, P.G., "A Model for Inhomogeneous Turbulent Flow," Proceedings of the Royal Society of London, A317, pp 417-433 (1970).

34. Saffman, P.G. and Wilcox, D.C., "Turbulence-Model Predictions for Turbulent Boundary Layers," AIAA J, 12, No 4, pp 541-546 (1974).

35. Wilcox, D.C. and Alber, I.E., "A Turbulence Model for High Speed Flows," Proceedings of the 1972 Heat Transfer and Fluid Mechanics Institute, Stanford Univ Press, pp 231-252 (1972).

36. Wilcox, D.C. and Traci, R.M., "A Complete Model of Turbulence," AIAA Paper No 76-351, AIAA 9th Fluid and Plasma Dynamics Conference, San Diego, Calif, (July 1976).

37. Traci, R.M. and Wilcox, D.C., "Freestream Turbulence Effects on Stagnation Point Heat Transfer," AIAA J, 13, No 7, pp 890-896 (1975).

38. Andersen, P.S., Kays, W.M. and Moffat, R.J., "The Turbulent Boundary Layer on a Porous Plate: An Experimental Study of the Fluid Mechanics for Adverse Free-Stream Pressure Gradients," Rept No HMT-15, Dept Mech Engr, Stanford Univ, Calif (1972).

39. Wilcox, D.C., "Turbulence-Model Transition Predictions for Blunt-Body Flows," AFOSR-TR-74-1714 (1974).

40. Nee, V.W. and Kovasznay, L.S.G., "Simple Phenomenological Theory of Turbulent Shear Flows," Physics of Fluids 12, p 473 (1969).